Highly Depleted Ethane and Mildly Depleted Methanol in Comet 21P/Giacobini-Zinner: Application of a New Empirical ν_2 Band Model for CH_3OH near 50 K

M. A. DiSanti[1,2], B. P. Bonev [1,3], G. L. Villanueva[1,3], M. J. Mumma[1,2]

Submitted to *The Astrophysical Journal*

10 May 2012

Number of Tables included: 3 (in main body) + 1 (in Appendix)

Number of Figures: 4

[1] Goddard Center for Astrobiology, Mail stop 693, NASA Goddard Space Flight Center, Greenbelt, MD, 20771, USA.

[2] Solar System Exploration Division, Mailstop 690, NASA Goddard Space Flight Center, Greenbelt, MD, 20771, USA.

[3] Department of Physics, Catholic University of America, Washington, DC 20064.

Direct correspondence to: michael.a.disanti@nasa.gov

Abstract

Infrared spectra of Comet 21P/Giacobini-Zinner (hereafter 21P/GZ) were obtained using NIRSPEC at Keck II on UT 2005 June 03, approximately one month before perihelion, that simultaneously measured H_2O, C_2H_6, and CH_3OH. For H_2O, the production rate of 3.8×10^{28} molecules s^{-1} was consistent with that measured during other apparitions of 21P/GZ retrieved from optical, infrared, and mm-wavelength observations. The water analysis also provided values for rotational temperature ($T_{rot} = 55^{+3}/_{-2}$ K) and the abundance ratio of ortho- and para-water (3.00±0.15, implying a spin temperature exceeding 50 K). Six Q-branches in the ν_7 band of C_2H_6 provided a production rate ($5.27 \pm 0.90 \times 10^{25}$ s^{-1}) that corresponded to an abundance ratio of 0.139 ± 0.024 % relative to H_2O, confirming the previously reported strong depletion of C_2H_6 from IR observations during the 1998 apparition, and in qualitative agreement with the depletion in C_2 known from optical studies. For CH_3OH, we applied our recently published *ab initio* model for the ν_3 band to obtain a rotational temperature ($48^{+10}/_{-7}$ K) consistent with that obtained for H_2O. In addition we applied a newly developed empirical model for the CH_3OH ν_2 band, and obtained a production rate consistent with that obtained from the ν_3 band. Combining results from both ν_2 and ν_3 bands provided a production rate ($47.5 \pm 4.4 \times 10^{25}$ s^{-1}) that corresponded to an abundance ratio of 1.25 ± 0.12 % relative to H_2O in 21P/GZ. Our study provides the first measure of primary volatile production rates for any Jupiter family comet over multiple apparitions using high resolution IR spectroscopy.

Keywords: spectroscopy, infrared, comets, composition

1. Introduction

Comet 21P/Giacobini-Zinner (hereafter 21P/GZ) was discovered in 1900 by Michel Giacobini, was re-discovered independently by Ernst Zinner in 1913, and was recovered in all apparitions since its discovery with the exception of the unfavorable ones in 1907, 1920, and 1953. Its Tisserand parameter with respect to Jupiter (T_J = 2.46) classifies 21P/GZ dynamically as a Jupiter Family comet (JFC), the predominant "feeding zone" for which is the scattered Kuiper disk, as predicted by the pre-eminent Nice model (Gomes et al. 2005, Morbidelli et al. 2008). This comet has the distinction of being the first to be visited by a spacecraft – in September 1985, the International Cometary Explorer (originally the International Sun-Earth Explorer-3) flew through its plasma tail, passing within 8,000 km of the nucleus. Here we report abundances of simultaneously observed C_2H_6, CH_3OH, and H_2O in 21P/GZ during its 2005 apparition, using the cross-dispersed high-resolution IR echelle spectrometer (NIRSPEC) at Keck II and applying our latest fluorescence models for H_2O, C_2H_6, and CH_3OH, including a new empirical model for the ν_2 band of CH_3OH.

Observational studies indicate substantial chemical diversity among comets (cf., Mumma and Charnley 2011, and references therein). The most comprehensive work reported optical narrow-band photometric observations of radical (photo-dissociation product) abundances spanning some three decades (A'Hearn et al. 1995). This survey established "typical" and "depleted" classes depending on their abundances of C_2 (and C_3) relative to CN and OH. It was argued this may reflect differences in carbon-chain chemistry (i.e., differing abundances of progenitor ices for C_2 and/or C_3), with inferred carbon-chain depletion being considerably more pronounced in JFCs compared with nearly isotropic comets (NICs; i.e., dynamically-new or long-period returning, from the Oort cloud) (see also Fink and Hicks 1996, Schleicher et al. 2007, Fink 2009, Cochran et al. 2012).

While highly diagnostic, these findings do not necessarily translate to a similar dichotomy in native ice abundances, primarily due to uncertainties in the parentages of fragmentation products (daughter or granddaughter species). Compared with optical observations, parent species have been studied in relatively few JFCs, owing mostly to their typically lower overall gas production relative to NICs. However, in recent years

advances in technology have permitted more detailed studies of JFCs in both radio (Biver et al. 2004; Crovisier et al. 2009) and infrared regimes (Weaver et al. 1999; Mumma et al. 2000, 2005, 2011; Dello Russo et al. 2007, 2008, 2009, 2011; DiSanti et al. 2007a; Kobayashi et al. 2007, 2010; Villanueva et al. 2006, 2011b; Paganini et al. 2012).

Through use of modern high-resolution spectrometers, the IR offers the unique capability of measuring trace gases simultaneously with H_2O, the most abundant volatile in comet nuclei and the principal driver of cometary activity for heliocentric distances (R_h) less than ~ 3 AU. Symmetric hydrocarbons (e.g., C_2H_2, CH_4, C_2H_6, etc.) have no electric dipole moment and so are not observable at radio wavelengths since pure rotational transitions are forbidden, leaving their infrared vibrational bands as the sole means of measuring their abundances in comets through remote sensing.

Comet 21P/GZ is often regarded as the prototypical carbon-chain depleted comet (A'Hearn et al. 1995). In this study we investigate whether its observed C_2 depletion carries over to primary (parent) volatiles, in particular to C_2H_6, which we quantify through application of a comprehensive fluorescence model for the ν_7 band near 3.35 μm (Villanueva et al. 2011a). We present a newly-developed empirical fluorescence model for CH_3OH, incorporating more than 100 lines in the ν_2 band that are interspersed with C_2H_6 ν_7 emissions. Application of our empirical g-factors for ν_2 together with our recently published *ab initio* quantum mechanical fluorescence model for the ν_3 band near 3.52 μm (Villanueva et al. 2012) enables us to retrieve a highly precise production rate for methanol in 21P/GZ.

We compare our results for 21P/GZ with those from the IR (for C_2H_6 and CH_3OH) and radio (for CH_3OH) during its most recent previous apparition in 1998. Our study represents the first such measure of parent volatile abundances at infrared wavelengths over multiple apparitions in any JFC. We also compare our abundances with those measured in other JFCs and with abundances of C_2 from optical studies. We end with a discussion of prospects for future studies of 21P/GZ, beginning with its next favorable apparition in 2018.

2. Observations and Data Processing

We obtained spectra of 21P/GZ on UT 2005 June 03.63 using the near-infrared cross-dispersed echelle spectrograph (NIRSPEC; McLean et al. 1998) on the 10-m Keck II telescope atop Mauna Kea, HI. NIRSPEC delivers simultaneous coverage of six echelle orders (at L-band) at sufficiently high spectral resolving power ($\lambda/\Delta\lambda \sim 25{,}000$) using a 3-pixel (0.43 arc-sec) wide slit to measure emission intensities of individual lines or groups of blended lines for a given molecule. One half-night (second half) was granted to obtain baseline measurements of Comet 9P/Tempel 1 approximately one month prior to the Deep Impact encounter. Comet 21P/GZ was accessible in the east toward the end of the night, permitting us to dedicate the final 40 minutes of available clock time to the study reported here. Because of this, and also due its modest brightness ($m_v = 10 - 12$), only one instrument setting was possible – this was chosen so as to simultaneously encompass C_2H_6 (in order 23), CH_3OH (orders 22 and 23), and H_2O (orders 26 and 27; see Table 1).

The telescope was nodded in our standard ABBA sequence, with each ABBA set representing four minutes of on-source integration time and with A- and B-beams each containing comet signal (the telescope was nodded by ±6 arc-seconds relative to the slit center for the two positions). For our observations, the slit was oriented at position angle 157° (Fig. 1A), approximately perpendicular to the Sun-comet direction (PA = 260°). A total of six ABBA sets (24 minutes on source) were obtained. Individual echelle orders were processed as described previously (Villanueva et al. 2011a; Bonev 2005; DiSanti et al. 2001; Mumma et al. 2001a).

Signals from A and B beams were combined, and spectra were extracted over 9 rows (1.78 arc-seconds) centered on the row containing peak molecular emission intensity in each order (Figs. 1B-1D; also see Table 2, note 'b'). The emission line spectrum was isolated by subtracting the cometary dust continuum convolved with the modeled atmospheric transmittance function (Figs. 2 through 4). Flux calibration was accomplished by obtaining spectra of an IR standard star (HR-5487). Absolute line fluxes were referred to the top-of-the atmosphere by ratioing measured line intensities to the monochromatic transmittance at each Doppler-shifted line-center frequency (based on

geocentric velocity Δ-dot = -5.42 km s^{-1}). Transmittances were modeled using the Line-By-Line Radiative Transfer Model (LBLRTM; Clough et al. 2005) and the latest HITRAN database with updated parameters (Rothman et al. 2010; see Villanueva et al. 2011a for detailed discussion and application). We used the NIRSPEC Slit-viewing CAMera (SCAM) to keep 21P/GZ in the slit, thereby ensuring that loss of flux (slit spillover) was due primarily to seeing. We quantified these losses when correcting our nucleus-centered production rates to global production rates (see §4.1).

3. Empirical Model for the ν_2 Band of CH_3OH

3.1 The Need for a ν_2 Band Model

Methanol is a molecule that is routinely observed in comets, both at IR and radio wavelengths. It has three fundamental vibrational bands in the 3.3 – 3.6 μm spectral region, ν_3 (parallel; symmetric CH_3 stretching mode, centered near 2844 cm^{-1}), ν_2, and ν_9 (predominantly perpendicular; asymmetric CH_3 stretching modes centered near 2990 and 2970 cm^{-1}, respectively). (The terms "parallel" and "perpendicular" refer, in the symmetric top approximation, to the orientation of the transition moment associated with the vibrational mode relative to the top axis; Herzberg 1945, p. 414.) Of these three bands, ν_3 has traditionally been targeted for measuring CH_3OH in comets, primarily because it is relatively free of blends with emissions from other species and also because it is spectrally more compact compared with the asymmetric bands, having a single strong, well-delineated Q-branch. The ν_2 and ν_9 bands (e.g., see Herzberg 1945, Fig. 128, p. 425) exhibit several sub-band Q-branches dispersed in frequency and interspersed with P- and R-branch lines (see §3.2).

In addition to providing an alternate means of quantifying CH_3OH in comets, the ability to interpret ν_2 band emissions has a practical application. Prior to the commissioning of NIRSPEC in 1999, the only available high-resolution IR spectrometer was CSHELL at the NASA-IRTF 3-m telescope (Tokunaga et al. 1990, Greene et al. 1994). This legacy instrument revolutionized the field of gas-phase spectroscopy at 1 – 5 μm, albeit with relatively small spectral coverage (within a single echelle order) per setting, for example only about 7 cm^{-1} in the "cometary organics" region (~ 3.3 – 3.6 μm). CSHELL is adequate for measuring the ν_3 Q-branch (having a total width of ~ 1.5 cm^{-1}), however this

required a dedicated, stand-alone setting for CH_3OH, and a second setting for measuring other parent molecules, for example C_2H_6 through its ν_7 band centered near 2985 cm^{-1}. A fluorescence model for the methanol ν_2 band permits prominent emission features of C_2H_6 and CH_3OH to be measured simultaneously, even for instruments with limited spectral grasp such as CSHELL. Although since superseded by NIRSPEC, and more recently by CRIRES at VLT (Käufl et al. 2004), the IRTF retains a unique niche by virtue of its daytime capability and its greater flexibility in scheduling observing time compared with VLT or Keck, further emphasizing the need for quantifying CH_3OH using ν_2 emissions. Regardless of the instrument, adequate interpretation of cometary spectra in the region from ~ 2970 – 3000 cm^{-1} requires disentangling emissions arising from different molecules, most notably C_2H_6 and CH_3OH, with lesser contributions from CH_4 and OH prompt emission. A major step involves characterizing CH_3OH in this region, and this is dominated by ν_2 band emission.

3.2 Aspects of our ν_2 Empirical Model

Toward this end, we developed an empirical model that includes 157 individual lines, with line assignments and frequencies adopted from jet-cooled laboratory spectra (Xu et al. 1997) and lower state energies taken from Mekhtiev et al. (1999). We incorporated approximately 70 percent of these (109 lines) to quantify CH_3OH in order 23 (see Fig. 3 and related discussion below). Details regarding our adopted notation, and results of our model as applied to 21P/GZ are given in the Appendix.

Fluorescence efficiencies (g-factors) for our empirical model are based on higher signal-to-noise spectra of the Halley Family Comet 8P/Tuttle, also observed with NIRSPEC. This comet exhibited a high abundance ratio CH_3OH/C_2H_6 (Bonev et al. 2008; also see Böhnhardt et al. 2008, Kobayashi et al. 2010), making it a good "template" for this study. Fig. 3A shows the resulting model compared with the 8P/Tuttle residuals from order 23. After accounting for emissions from other species (specifically C_2H_6, CH_4 and OH prompt emission), we judiciously identified 18 separate spectral intervals in which identified CH_3OH ν_2 emissions are isolated (see Appendix). Values for our empirical g-factors were assigned such that the production rate for each interval, based on a 9-row extract centered on the nucleus ($Q_{nc,int}$; see Eq. 2 below), agreed with that obtained

independently from application (to 8P/Tuttle) of our *ab initio* quantum model for the simultaneously observed ν_3 band in order 22 (Villanueva et al. 2012)[1]. These g-factors were then applied to the 21P/GZ residuals (after accounting for C_2H_6 and OH emissions;[2] Figs. 3B-3C). Results for each spectral interval are presented in Table A1.

4. Production Rates and Molecular Abundances

4.1 Methodology for Measuring Production Rates in 21P/GZ

Global (or total) production rates (Q_{tot}) for parent molecules were calculated using our well-documented methodology (Villanueva et al. 2011a, Bonev 2005, Mumma et al. 2003, DiSanti et al. 2001). In applying our formalism, we measure a growth factor (GF), relating Q_{tot} for a primary volatile to that based on a 9-row extract centered on the peak emission intensity (the "nucleus-centered" production rate, Q_{nc}):

$$Q_{tot} \equiv Q_{nc} GF. \qquad (1)$$

The growth factor GF (> 1) corrects for loss of flux, due primarily to atmospheric seeing as explained in §2. In our analysis of 21P/GZ, the spectral regions (intervals) we selected for determining our production rates typically consisted of blends of multiple lines. Within each chosen interval, Q_{nc} for that interval (denoted $Q_{nc,int}$) is proportional to the measured line flux (F_{int}, W m^{-2}), divided by the product of rest frequency (ν_i, cm^{-1}), fluorescence g-factor ($g_{1,i}$, photon s^{-1} molecule^{-1}, evaluated at R_h = 1 AU), and atmospheric transmittance (T_i) at the Doppler-shifted frequency for each encompassed line, summed over all contributing lines (numbering 'n'):[3]

---

[1] The production rate for CH_3OH initially published for 8P/Tuttle (Q_{tot} = 49.65 x 10^{25} molecules s^{-1}; Bonev et al. 2008) was based on Q_{nc} = 33.1 x 10^{25} s^{-1} (using the ν_3 Q-branch intensity) combined with a slit loss correction factor (GF) of 1.5. The value obtained using the new band model for ν_3 as presented in Villanueva et al. (2012) revises Q_{nc} downward by ~ 12 percent, to 29.0 x 10^{25} s^{-1}.

[2] Due to its small geocentric Doppler shift at the time of our observations (-5.42 km s^{-1}), CH_4 was not observable in 21P/G-Z due to severe extinction by corresponding telluric absorption.

[3] For the case of only one line within an interval, the quantity in square brackets in Eq. 2 is equivalent to $(F_{line}/T)/(\nu_{line}\, g_{line,1AU})$, where F_{line}/T is the top-of-atmosphere line flux as described in §2.

$$Q_{nc,int} = \frac{4\pi\Delta^2}{hc\ \tau_1 f(x)} \left| \frac{F_{int}}{\sum_{i=1}^{n} \nu_i g_{1,i} T_i} \right|. \quad (2)$$

In Eq. 2, τ_1 (s) is the photo-dissociation lifetime at R_h = 1 AU, f(x) is the fraction of all molecules in the coma contained in the nucleus-centered beam (assuming native release and spherically-symmetric outflow; see Appendix in Hoban et al. 1991), Δ is expressed in meters, and hc = 1.99 x 10^{-23} W s cm. The overall Q_{nc} represents the mean of values from all intervals, weighted by their respective stochastic errors. For CH_3OH in order 23, the uncertainty in our equivalent empirical g-factor for each interval is also included in this weighting (Table A1).

We calculate our global production rates using GF = 1.62 (Table 2), based on the spatial emission profile summed from several bright water lines (Fig. 1A). Although noisier, the GF for CH_3OH was in agreement with this value, and that for C_2H_6, although somewhat larger, was also consistent (within 1σ uncertainty) with that measured for H_2O. Details are given in Table 2 (in particular, see note d).

4.2. Results for Individual molecules

4.2.1. H_2O

A total of 31 water lines contained within 24 spectral intervals were measured in orders 26 and 27 (Fig. 2). These sample a sufficiently large range in rotational energy (> 300 cm^{-1}; see inset to Fig. 2) to allow determination of the rotational temperature with extremely high precision (T_{rot} = $55^{+3}/_{-2}$ K). Of the encompassed lines, 18 are ortho (parallel nuclear spins of the two H-atoms), and 13 are para (anti-parallel spins). Analysis of their relative intensities allowed an accurate measure of an ortho-to-para ratio (OPR, 3.00 ± 0.15) that is consistent with equilibrated spins, thereby implying a spin temperature (T_{spin}) exceeding 50 K (e.g., see Bonev et al. 2007). Our method for decoupling T_{rot} and T_{spin} provides a highly precise (and accurate) measure of the global production rate for H_2O ($Q(H_2O)$, 3.800 ± 0.088 x 10^{28} molecules s^{-1}).

4.2.2. OH Prompt Emission

Our observations encompass four strong lines of OH in order 23 (Fig. 3). These lines arise through "prompt emission" in the v = 1 – 0 band, radiating within milliseconds from vibrationally and rotationally excited states following their production from photo-dissociation of H_2O molecules in the coma (Bonev et al. 2006, Bonev and Mumma 2006, Mumma et al. 2001a). Empirical g-factors for more than 20 OH prompt emission lines (denoted OH*) from v = 1 – 0 and 2 – 1 bands were derived from NIRSPEC spectra of two comets (C/2000 WM1 LINEAR and C/2004 Q2 Machholz; Bonev et al. 2006).

However, such a study is problematic for the lines observed here, in that these are interspersed with emissions from C_2H_6, CH_3OH, and perhaps other species. In particular, our effort to obtain accurate production rates in 21P/GZ, both for C_2H_6 and for CH_3OH in order 23 is hampered by uncertainties in the g-factor for the OH P12.5 2^- line at rest frequency 2996.892 cm^{-1}. This line is blended with C_2H_6 $^rQ_3$, and also with the strong $A^{+->-}$(K=1->0) Q-branch of the CH_3OH ν_2 band (plus a few weaker ν_2 lines; see Table A1). There are three reasons for this uncertainty in g-factor: (1) The spectrally confused nature of this region precludes isolating the contribution from OH*, and so requires interpolation/extrapolation from line g-factors measured from other "quadruplets" such as those near 3045 and 2785 cm^{-1}; (2) the intensities of OH* lines depend on the details of water excitation and subsequent uni-molecular dissociation (e.g., on the ratio of solar Ly α to UV-continuum ratio; see discussion in §4 of Bonev et al. 2006; see also Bonev and Mumma 2006 and references therein). Consequently, it is not known how well the value for the P12.5 2^- line in 8P/Tuttle applies to 21P/GZ, observed approximately 2.5 years earlier; and (3) in 21P/GZ, maximum line intensities for C_2H_6 and CH_3OH were obtained from spectral extracts displaced slightly from those for H_2O (see Table 2, note 'b'); this introduces additional uncertainty in scaling the modeled OH* contribution.

Nonetheless we estimated their effective g-factors through comparison with OH lines from adjacent multiplets. We also estimated the g-factor for P12.5 2^- empirically from NIRSPEC observations of Comet C/1999 S4 (LINEAR) in July 2000. This comet was very highly depleted in virtually all primary volatiles, including C_2H_6 and CH_3OH (Mumma et al. 2001b), leaving the OH* lines as the only discernable emissions in excess

of the continuum in order 23. These two independent approaches led to g-factors for the P12.5 2$^-$ line in the ratio 1.19 (the one based on LINEAR S4 being larger), exemplifying the uncertainties associated with obtaining accurate g-factors for these lines when comparing comets observed at different times. Based on this discussion, we exclude this region in calculating our "most probable" production rates and mixing ratios for C_2H_6 and CH_3OH; however, including signal in this region does not alter our conclusions regarding the abundances of C_2H_6 and CH_3OH (see below, and Tables 2 and 3).

4.2.3. C_2H_6

Order 23 is dominated by emissions from ethane (ν_7 band) and methanol (primarily the ν_2 band). One motivation for our study of 21P/GZ is to investigate (and, in the case of C_2H_6, to confirm) whether the depletion of C_2 observed in this comet (A'Hearn et al. 1995; Fink 2009) carries over to parent molecules. Depleted C_2H_6 was reported from CSHELL observations of 21P/GZ during the 1998 apparition (Weaver et al. 1999; Mumma et al. 2000; see §5.1.2). This might be expected if acetylene (C_2H_2) is the dominant source of C_2, as the most efficient means of producing C_2H_6 is H-atom addition to C_2H_2 on the surfaces of interstellar icy grains at low temperatures (Mumma and Charnley 2011; Rodgers and Charnley 1998; also see §6).

We obtained production rates from the intensities of seven Q-branches of the C_2H_6 ν_7 band: $^rQ_3$, $^rQ_2$, $^rQ_1$, $^rQ_0$, $^pQ_1$, $^pQ_2$, $^pQ_3$, and identify these by numbers 1 – 7, respectively, in Fig. 3B. Our production rates were based on a full quantum model for the ν_7 band of C_2H_6 that includes P- and R-branch intensities and contributions from the $\nu_7+\nu_4-\nu_4$ combination band (Villanueva et al., 2011a). Because each Q-branch samples a range of rotational energies, and because there is considerable overlap in the energies sampled among these Q-branches, the resulting production rate is relatively insensitive to T_{rot}. For this reason, we adopt T_{rot} = 50 K for C_2H_6. This temperature falls between those we measured for H_2O and for CH_3OH (based on analysis of the ν_3 band; see §4.2.4.1 and Fig. 4).

Global production rates for the seven Q-branches were calculated using their integrated line fluxes and applying the growth factor measured for H_2O (= 1.62); these are indicated

in Fig. 3D. However, because the g-factor for the blended P12.5 2⁻ prompt emission line of OH is uncertain (§4.2.2), $^{r}Q_3$ is excluded from our quantitative analysis of C_2H_6. The mean global production rate is then the mean of the remaining six points, weighted by their individual stochastic uncertainties (denoted by the error bars in Fig. 3D). We obtained a global production rate ($Q(C_2H_6)$, $5.27 \pm 0.90 \times 10^{25}$ s^{-1}) that translates to an abundance ratio of $(0.139 \pm 0.024) \times 10^{-2}$ relative to H_2O (Tables 2 and 3). This is well below the current "normal" value (~ 0.6%; Bockelée-Morvan et al. 2005, DiSanti and Mumma 2008, Mumma and Charnley 2011), confirming highly depleted C_2H_6 in 21P/GZ and commensurate with its observed C_2 depletion (A'Hearn et al. 1995, Fink 2009; see also Table 3).

4.2.4. CH_3OH

4.2.4.1. Rotational Temperature and Abundance for CH_3OH from Order 22

We identified 36 spectral intervals in order 22 and, applying our new ν_3 band model (Villanueva et al. 2012), we measured a rotational temperature for CH_3OH ($T_{rot} = 48^{+10}/_{-7}$ K; Fig. 4) consistent with that measured for H_2O in 21P/GZ. Our production rate for CH_3OH from order 22 ($4.63 \pm 0.55 \times 10^{26}$ s^{-1}) translates to an abundance ratio of $(1.22 \pm 0.15) \times 10^{-2}$ with respect to H_2O (Table 3).

4.2.4.2. CH_3OH in Order 23 – Results using our Empirical Model for the ν_2 Band

Subtracting modeled C_2H_6 (and OH*) emissions from the (continuum-subtracted) residuals (Fig. 3B) results in a net emission spectrum dominated by methanol (labeled "CH_3OH residuals" in Fig. 3C). Comparison with our empirical model provides an additional measure of CH_3OH production. In Fig. 3E we show the resulting global production rates for CH_3OH in 21P/GZ based on signal contained in each of the 18 spectral intervals in order 23. The mean of these (excluding interval 5; see §4.2.2) results in $Q(CH_3OH) = (4.88 \pm 0.71) \times 10^{26}$ s^{-1} and therefore an abundance ratio of $(1.28 \pm 0.19) \times 10^{-2}$ based on CH_3OH in order 23 alone. (Including interval 5 results in an abundance ratio of $(1.06 \pm 0.17) \times 10^{-2}$.) Combining CH_3OH from orders 22 and 23 (but excluding interval 5) results in $Q_{tot}(CH_3OH) = (47.5 \pm 4.4) \times 10^{25}$ s^{-1}, or $(1.25 \pm 0.12) \times 10^{-2}$ relative to H_2O.

5. Abundance Comparisons

5.1. Comparisons with Other 21P/GZ Observations

5.1.1. Water Production

The global production rate we measure for H_2O in 21P/GZ (3.8, expressed in 10^{28} molecules s^{-1}) compares favorably with the values reported elsewhere. In their optical photometric survey, A'Hearn et al. (1995) give $Q_{OH} = 3.2$ (corresponding to $Q_{H2O} \sim 3.5$) at the same heliocentric distance as our 2005 observations ($R_h = 1.12$ AU), and A'Hearn et al. estimated 4.2 for the maximum Q_{H2O} at perihelion ($R_h = 1.03$ AU). Fink (2009) lists a range (1.6 – 4.2) from optical spectra encompassing $1.05 < R_h < 1.21$ AU during the 1985 apparition. Weaver et al. (1999) measured $Q_{H2O} \sim 2 - 3$ from 1998 for $1.05 < R_h < 1.11$ AU based on IR spectra using CSHELL. Crovisier et al. (2002) report a maximum $Q_{H2O} = 5.1$ at $R_h = 1.05$ AU, and Crovisier et al. (2009) report $Q_{H2O} = 3$ at $R_h = 1.2$ AU, based on observations of OH from Nançay during the 1998 apparition.

5.1.2. Infrared Observations of C_2H_6 and CH_3OH in 21P/GZ

Highly depleted C_2H_6 in 21P/GZ was reported in two papers from the 1998 apparition based on observations with CSHELL. Mumma et al. (2000) reported an abundance ratio (C_2H_6/H_2O, $0.22 \pm 0.13 \times 10^{-2}$) that is consistent with ours, albeit with larger uncertainty due to the lower sensitivity afforded by CSHELL compared with NIRSPEC. Weaver et al. (1999) reported a range of (3σ) upper limits, the maximum of their range (0.08×10^{-2}) being only ~ 60 percent of our value (0.14×10^{-2}; Table 3). Taken together, these two papers suggested possible compositional heterogeneity in 21P/GZ. Our observed differences in spatial profiles for H_2O, C_2H_6, and CH_3OH (Fig. 1) may result from compositional differences among source regions on the nucleus. (However, given the relatively poor signal-to-noise in our profiles for ethane and methanol, and without detailed knowledge concerning the release of material, definitive conclusions cannot be drawn.) For methanol, Weaver et al. reported a range for the abundance ratio ($0.9 - 1.4 \times 10^{-2}$) based on the entire ν_3 band intensity and $g_{band} = 1.5 \times 10^{-4}$ photon s^{-1} $molecule^{-1}$. This encompasses our combined value of $(1.25 \pm 0.12) \times 10^{-2}$ (from orders 22 and 23), as

well as our values from each order separately, and even our value of $(1.12 \pm 0.11) \times 10^{-2}$ when interval 5 in order 23 is included in our two-order mean CH_3OH abundance.

5.1.3. Millimeter Observations of CH_3OH in 21P/GZ

Biver et al. (2002) included 21P/GZ in a survey of molecular abundances in 24 comets based on millimeter wavelength observations with the Institut de Radio Astronomie Millimetrique (IRAM) 30-m and other radio telescopes. For CH_3OH they reported an abundance ratio $(1.6 \pm 0.4 \times 10^{-2})$ that implied a range $Q_{CH3OH} \sim (3.6 - 10) \times 10^{26}$ molecules s^{-1}, considering their $\pm 1\sigma$ extremes in abundance along with the range in Q_{H2O} from the Nançay observations $(3 - 5.1 \times 10^{28}$ molecules s^{-1}; see §5.1.1). Based on this, our measured abundance for CH_3OH falls near the low end of the IRAM 1σ limit. The agreement between these results and our measurements is notable, especially considering that the radio measurements of CH_3OH and OH were conducted with different telescopes having greatly different beam sizes whose results represent temporal release averaged over widely different intervals, whereas our NIRSPEC observations measured both CH_3OH and H_2O simultaneously and in the same well-characterized (small) beam.

5.2. Abundance Comparisons of C_2H_6 and CH_3OH Among Jupiter Family Comets

An ensemble of comets (both NICs and JFCs) measured with IR spectroscopy reveals an emerging taxonomy based on the diversity of primary volatile abundances (specifically C_2H_6, CH_3OH, C_2H_2, and HCN) among its members. Seven of 14 comets measured through 2008 are conditionally classified "organics-normal," while two are "enriched" and two are "depleted," particularly regarding their abundances of C_2H_6 and CH_3OH, for which "normal" values are, respectively, approximately 0.6 and 2 percent relative to H_2O (e.g., see Fig. 8 in Mumma and Charnley 2011). A key question regards the extent to which comets fall into these three categories as opposed to forming a more continuous distribution in volatile organic compositions, and also whether the extreme examples (both enriched and depleted) represent end members or even if the "normal" group reflects a representative mean composition. Indeed, this classification scheme is being challenged as additional comets are characterized. For example, neither 8P/Tuttle (Böhnhardt et al. 2008, Bonev et al. 2008, Kobayashi et al. 2010) nor C/2007 N3 (Lulin) (Gibb et al. 2012) fit neatly into any of the three categories.

The overall sample is dominated by NICs (delivered from the Oort cloud), however the JFC population (primarily from the scattered Kuiper disk) contributes in significant ways. An important finding revealed even in this relatively small sample of comets is that members from NIC and JFC populations are present both in enriched and depleted categories, as predicted by the Nice model (Gomes et al. 2005, Morbidelli et al. 2008).

Table 3 exemplifies this through abundance comparisons among JFCs. Comet 17P/Holmes is clearly enriched (Dello Russo et al. 2008) and 73P/Schwassmann-Wachmann 3 is depleted (Villanueva et al. 2006; Dello Russo et al. 2007) in both C_2H_6 and CH_3OH, while 10P/Tempel 2 (Paganini et al. 2012) showed mild depletions in both, as did 9P/Tempel 1 (except for the material ejected by the Deep Impact event, which revealed "normal" C_2H_6; Mumma et al. 2005, DiSanti et al. 2007b). Comet 21P/GZ was highly depleted in C_2H_6 yet had only mildly depleted (to nearly normal) CH_3OH, 6P/d'Arrest (Dello Russo et al. 2009) had mildly depleted C_2H_6 and normal CH_3OH, while in 103P/Hartley 2 both molecules had abundances consistent with normal (Mumma et al. 2011; Dello Russo et al. 2011; Kawakita et al. 2012). Clearly there are examples that do not fit the proposed relatively simple three-tiered classification scheme, even based on this small sample of seven JFCs.

5.3. Comparisons with C_2 Abundances from Optical Observations of JFCs

An additional comparison involves the potential relation between primary volatile abundances (in particular C_2H_6 for the present study) and C_2. In an initial optical survey (A'Hearn et al. 1995), approximately one-third of 85 comets were classified as "carbon-chain depleted," with this classification being considerably more pronounced in JFCs compared with NICs. This dichotomy with dynamical class is reinforced by other surveys (Fink and Hicks 1996, Fink 2009, Cochran et al. 2012), including an extensive taxonomic compilation of well over 100 comets that identifies up to nine compositional groupings when abundances of NH, a potentially important tracer for NH_3, are included (Schleicher et al. 2007).

Five of seven comets in Table 3 have fairly similar values for the ratio C_2H_6/C_2. One exception is 17P/Holmes, however measurements of both C_2H_6 and C_2 were obtained following its spectacular outburst in October 2007, and so uncertainties associated with a

rapidly evolving coma might be expected. This leaves 6P/d'Arrest as a notable outlier, with mild depletion of C_2H_6 (by approximately a factor of 2 relative to "normal") but C_2 near the midpoint of the range for comets classified as "typical" by A'Hearn et al. (1995).

While the majority of JFCs in Table 3 exhibit similar C_2H_6/C_2, the inter-relationship between these two species is far from secure. C_2 is produced directly from C_2H_2 with a branching ratio of approximately 20 percent (Huebner et al. 1992), but some comets produce more C_2 than can be accounted for by C_2H_2 alone, for example 8P/Tuttle (Bonev et al. 2008) and C/2007 N3 (Lulin) (Gibb et al. 2012), both of which were depleted in C_2H_2. An analogous situation may hold for the JFC 6P/d'Arrest, with strongly depleted C_2H_2 (< 0.052 %, 3σ) suggesting the need for an additional source of C_2, and similarly one or more additional sources for CN by virtue of its larger abundance compared with that of HCN (Dello Russo et al. 2009).

In order to reproduce observed profiles of C_2 in Comet 1P/Halley, Combi and Fink (1997) investigated CHON grains as a possible additional source, and Klavetter and A'Hearn (1994) found that ~ 50 % of CN in the coma of 1P/Halley originated from jets of CHON origin. Lederer et al. (2009) proposed sub-micron organic grains (e.g., CHON) to explain OH, CN, and C_2 jets in C/1995 O1 (Hale-Bopp), and Frey et al. (2005) proposed additional sources of C_2 in comets, including photo-degradation of CH_3CN, HC_3N, and C_2N_2.

Photo-dissociation of C_2H_6 can lead to C_2, however multiple steps are required (including production of C_2H_2) and branching ratios are highly uncertain (Helbert et al. 2005, Kobayashi et al. 2010). Indeed, Weiler (2012) compared radial column densities of C_2 and C_3 observed in three comets with a coma chemistry model, and concluded that C_2H_6 is not a significant parent of C_2. The similar values for C_2H_6/C_2 among five of the seven JFCs in Table 3 may be coincidental, or could indicate a common source of (and efficiency for producing) C_2 and C_2H_6 (such as C_2H_2) that dominates contributions from alternative sources (e.g., CHON) in these five comets. The problem of relating abundances of fragment species to potential parents is not resolved, and parentages may vary among comets. Clearly, in general both gas and grain sources need to be considered.

6. Production of C_2H_6 and CH_3OH through Grain Surface Chemistry

Infrared measurements such as those presented here can provide information on conditions in the environment where comets formed. Because gas phase formation of C_2H_6 is highly inefficient, a mechanism was proposed (Tielens 1992) involving H-atom addition reactions to C_2H_2 on the surfaces of interstellar grains, and this was later borne out by the discovery of abundant C_2H_6 in comet C/1996 B2 (Hyakutake) (Mumma et al. 1996) and through further theoretical development (Rodgers and Charnley 1998). The now-routine measurement of C_2H_6 in comets suggests such processing is ubiquitous in pre-cometary environments.

Similarly, gas-phase formation of CH_3OH, through reaction of the methyl ion (CH_3^+) with water followed by dissociative recombination of the product species ($CH_3OH_2^+$), cannot explain observed abundances of CH_3OH in interstellar sources (Geppert et al. 2006; Garrod et al. 2006; Wirström et al. 2011). In addition, chemical models that trace the evolution of material from dark molecular clouds through proto-planetary disks have not found a viable formation pathway for CH_3OH in the gas phase (Walsh et al. 2010; Willacy & Woods 2009; Willacy 2007). However, in analogy with C_2H_6, methanol is efficiently synthesized through grain surface chemistry in sufficiently cold environments. Hydrogenation of CO condensed onto grains, as simulated by laboratory irradiation experiments on pure CO ice and CO/H_2O ice mixtures at very low temperatures (~ 10 – 20 K), show this to be an efficient means of producing CH_3OH (Hudson and Moore 1999, Hiraoka et al. 2002, Watanabe et al. 2004).

7. Implications for Future Studies of 21P/Giacobini-Zinner

In this context, our measurements of strongly depleted C_2H_6 but only modestly depleted CH_3OH in 21P/GZ lead naturally to questions regarding its abundances of C_2H_2 and CO. Weaver et al. (1999) reported an abundance of $C_2H_2/H_2O < 0.3 – 0.4$ % (3σ), which does not represent a sensitive upper limit given the (current) "normal" abundance of C_2H_2 among comets (~ 0.2 – 0.3 %; Mumma and Charnley 2011, DiSanti and Mumma 2008, Bockelée-Morvan et al. 2005). Mumma et al. (2000) reported a high abundance ratio

CO/H_2O (~ 10 %), however this was based on a marginal detection of H_2O (below 2σ) together with an abundance ratio $C_2H_6/CO = 2.1 \pm 0.6$ %. Our current result for C_2H_6 (0.139 ± 0.024 %) implies an abundance ratio $CO/H_2O = 6.6 \pm 1.1$ %, if scaled from the Mumma et al. (2000) ratio for C_2H_6/CO. Results from these two studies (Mumma et al., Weaver et al.), conducted approximately three weeks apart, are at odds. In the latter work H_2O was detected yet neither C_2H_6 *nor* CO were seen, and both papers mentioned compositional heterogeneity as a possible explanation for these differences. Assuming a (modest) R_h^{-2} dependence, the upper limit reported for Q(CO) at $R_h = 2.4$ AU from 2005 Spitzer observations of 21P/GZ (6.0×10^{26} molecules s^{-1}; Pittichová et al. 2008) scales to ~ 2.8×10^{27} molecules s^{-1} at $R_h = 1.12$ AU (corresponding to the observations reported here). Based on our measured $Q(H_2O)$ (3.8×10^{28} molecules s^{-1}), this corresponds to $CO/H_2O < 7.3$ %, consistent with the revised Mumma et al. value (6.6 %).

Because of its short orbital period (6.6 years), apparitions of 21P/GZ provide widely varying observational opportunities. This is particularly true when comparing the apparitions in 2012 and 2018. Near perihelion, the geocentric distance Δ was > 1.8 AU in 2012, but will be only ~ 0.4 AU in 2018. Moreover, the geocentric velocity in 2018 exceeds 10 km s^{-1} when Δ reaches ~ 0.48 AU (and thus is adequate for studying CO and CH_4). Assuming gas production rates (and rotational temperatures) similar to those measured in previous apparitions, line intensities in 2018 are expected to be larger by factors of three to four compared with those observed in 2005, and by factors of two to three compared with those from 1998 (for which Δ ~ 0.9 – 1.1 AU). Combined with anticipated improvements in instrumentation (e.g., higher spectral resolving power and sensitivity), the 2018 apparition will enable deep searches for trace species – e.g., detection of C_2H_2 or, if severely depleted, establishing stringent upper limits for its abundance – and will allow the question of potential compositional heterogeneity in the nucleus to be addressed in considerable detail.

8. Conclusions

We used NIRSPEC at Keck II to obtain infrared spectra of 21P/GZ on UT 2005 June 03.6 that allowed a simultaneous measure of H_2O, C_2H_6, and CH_3OH. For H_2O, we obtained a production rate (3.8×10^{28} molecules s^{-1}) consistent with that measured during

earlier apparitions of 21P/GZ as retrieved from optical, IR, and mm-wavelength observations. Our water analysis also provided consistent values for rotational temperature (T_{rot}, $55^{+3}/_{-2}$ K) and spin temperature (T_{spin}, > 50 K, based on OPR 3.00 ± 0.15).

Our results confirm strongly depleted C_2H_6 and mildly depleted CH_3OH in 21P/GZ, as reported previously from observations during the 1998 apparition. For C_2H_6 we applied our *ab intio* quantum mechanical fluorescence model for the ν_7 band that includes contributions from the Q-, P-, and R-branches and also from a combination band. For CH_3OH, we applied our recently published *ab initio* model for the ν_3 band to obtain a rotational temperature (T_{rot}, $48^{+10}/_{-7}$ K) consistent with the value we measured for H_2O. The first application of our newly developed empirical model for the CH_3OH ν_2 band provided a production rate consistent with that obtained from ν_3. Combining analyses of both bands (ν_2 and ν_3) permitted a ~ 10σ detection of CH_3OH in 21P/GZ. Our study represents the first measure of primary volatile abundances from ground-based IR spectroscopy for any JFC over multiple apparitions. It also provides a comparator for more extensive studies of 21P/GZ in future apparitions, beginning with that in 2018.

Acknowledgements

MAD and GLV acknowledge support from NASA's Planetary Atmospheres Program (RTOP 09-PATM09-0080; PI MAD and 08-PATM-0031; PI GLV). BPB acknowledges support from the NSF Astronomy and Astrophysics Grants Program (AST-0807939). We also acknowledge support from NASA's Planetary Astronomy Program for MAD (RTOP 09-PAST09-0034) and for MJM, GLV, and BPB (RTOPs 344-32-07, 08-PAST08-0033/34), and from NASA's Astrobiology Program through the NASA Astrobiology Institute (RTOP 344-53-51; PI MJM). The data presented herein were obtained at the W. M. Keck Observatory, operated as a scientific partnership among CalTech, UCLA, and NASA. This Observatory was made possible by the generous financial support of the W. M. Keck Foundation. The authors wish to recognize and acknowledge the very significant cultural role and reverence that the summit of Mauna

Kea has always had within the indigenous Hawaiian community. We are most fortunate to have the opportunity to conduct observations from this mountain.

References

A'Hearn, M. F., Millis, R. L., Schleicher, D. G., Osip, D. J., & Birch, P. V. 1995, Icarus, 118, 223

Biver, N., Bockelée-Morvan, D., Crovsier, J., Colom, P., et al. 2002, EMP, 90, 323

Bockelée-Morvan, D., Crovisier, J., Mumma, M. J., & Weaver, H. A. 2005, *in* Comets II (Eds. M. C. Festou, H. U. Keller, H. A. Weaver), Univ. Arizona Press, Tucson

Böhnhardt, H., Mumma, M. J., Villanueva, G. L., et al. 2008, ApJ, 683, 171

Bonev, B. P., & Mumma, M. J. 2006, ApJ, 653, 788

Bonev, B. P., Mumma, M. J., DiSanti, M. A., Dello Russo, N., Magee-Sauer, K., Ellis, R. S., & Stark, D. P. 2006, ApJ, 653, 774

Bonev, B. P., Mumma, M. J., Radeva, Y. L., DiSanti, M. A., Gibb, E. L., & Villanueva, G. L. 2008, ApJ (Lett), 680, L61

Bonev, B.P. 2005, PhD Thesis, The University of Toledo

Clough, S. A., Shephard, M.W., Mlawer, E. J., et al. 2005, J. Quant. Spectrosc. Radiat. Transfer, 91, 233

Cochran, A. L., Barker, E. S., & Gray, C. L. 2012, Icarus, 218, 144

Combi, M. R., & Fink, U. 1997, ApJ, 484, 879

Crovisier, J., Colom, P., Gérard, É., Bockelée-Morvan, D., Henry, F., Lecacheux, A., & Biver, N. 2002, in Proc. Asteroids, Comets, Meteors – ACM 2002 (Ed. B. Warmbein), ESA SP-500, p. 685.

Crovsier, J., Biver, N., Bockelée-Morvan, D., Boissier, J., Colom, P., & Lis, D. C. 2009, EMP, 105, 267

Dello Russo, N., Vervack, R. J., Jr., Kawakita, H., Kobayashi, H, Biver, N., Bockelée-Morvan, D., & Crovisier, J. 2009, ApJ, 703, 187

Dello Russo, N., Vervack, R. J., Jr., Weaver, H. A., Biver, N., Bockelée-Morvan, D., Crovisier, J., & Lisse, C. M. 2007, Nature, 448, 172

Dello Russo, N., Vervack, R. J., Jr., Weaver, H. A., Montgomery, M. M., Deshpande, R., Fernandez, Y. R., & Martin, E. L. 2008, ApJ, 680, 793

Dello Russo, N., Vervack, R. J., Jr., Lisse, C. M., Weaver, H. A., Kawakita, H., et al. 2011, ApJ, 734, L8

DiSanti, M. A., Bonev, B. P., Magee-Sauer, K., Dello Russo, N., Reuter, D. C., Mumma, M. J., & Villanueva G. L. 2006, ApJ, 650, 470

DiSanti, M. A., & Mumma, M. J. 2008, Sp. Sci. Rev., 138, 127

DiSanti, M. A., Anderson, W. M., Villanueva, G. L., Bonev, B. P., Magee-Sauer, K., Gibb, E. L., & Mumma, M. J. 2007a, ApJ, 661, L101

DiSanti, M. A., Villanueva, G. L., Bonev, B. P., Magee-Sauer, K., Lyke, J. E., & Mumma, M. J. 2007b, Icarus, 187, 240

DiSanti, M.A., Mumma, M.J., Dello Russo, N. & Magee-Sauer, K. 2001, Icarus, 153 (2), 361

Fink, U. 2009, Icarus, 209, 311

Fink, U., & Hicks, M. D. 1996, ApJ, 459, 729

Frey, N., Bénilan, Y., Cottin, H., Gazeau, M.-C., & Crovisier, J. 2005, Plent. Sp. Sci. 53, 1243

Garrod, R., Park, I. H., Caselli, P., & Herbst, E. 2006, Faraday Disc., 133, 51

Geppert, W. D., Hamberg, M., Thomas, R. D., Osterdahl, F., Hellberg, F., et al. 2006, Faraday Disc., 133, 177G

Gibb, E. L., Bonev, B. P., Villanueva, G. L., DiSanti, M. A., Mumma, M. J., Sudholt, E., & Radeva, Y. L. 2012, ApJ, 749, 1

Gomes, R., H.F. Levison, K. Tsiganis, & A. Morbidelli 2005, Nature, 435, 466

Green, T. P., Tokunaga, A. T., & Carr, J. S. 1994, *in* Infrared Astronomy with Arrays: The Next Generation (Ed: McLean, I.), Kluwer Press, p. 511

Helbert, J., Rauer, H., Boice, D. C., & Huebner, W. F. 2005, Astron. Astrophys., 442, 1007

Herzberg, G. 1945, Infrared and Raman Spectra of Polyatomic Molecules,Vol. II, Molecular Spectra and Molecular Spectra (New York: Van Nostrand Company)

Hiraoka, K., Sato, T., Sato, S., Sogoshi, N., Yokoyama, T., Takashima, H., Kitagawa, S. 2002, ApJ, 577(1), 265

Hoban, S., Mumma, M. J., Reuter, D. C., DiSanti, M., A., Joyce, R., & Storrs, A. 1991, Icarus, 93, 122

Hudson, R. L., & Moore, M. H. 1999, Icarus, 140, 451

Huebner, W. F., Keady, J. J., & Lyon, S. P. 1992, Astron. Sp. Sci., 195, 1

Käufl, H., et al. 2004, Proc. SPIE, 5492, 1218

Kawakita, H., et al. 2012, Icarus (submitted)

Klavetter, J. J., & A'Hearn, M. F. 1994, Icarus, 107, 322

Kobayashi, H., Kawakita, H., Mumma, M. J., Bonev, B. P., Watanabe, J-I, & Fuse, T. 2007, ApJ, 668, L75

Kobayashi, H., Bockelée-Morvan, D., Kawakita, H., Dello Russo, N., et al. 2010, A&A, 509, A80.

McLean, I. S., et al. 1998, Proc. SPIE, 3354, 566

Mekhtiev, M. A., Godfrey, P. D., & Hougen, J. T. 1999, J. Mol. Spectrosc., 194, 171

Morbidelli A., Levison, H. F., & Gomes, R. 2008, *in* The Solar System Beyond Neptune, eds. M. A. Barucci, H. Böhnhardt, D. P. Cruikshank, A. Morbidelli, p. 275. Tucson: Univ. Ariz. Press

Mumma, M. J., & Charnley, S. B. 2011, Ann. Rev. Astron. Astrophys., 49, 471

Mumma, M. J., Bonev, B. P., Villanueva, G. L., Paganini, L., DiSanti, M. A., et al. 2011, ApJ, 734, L7

Mumma, M. J., Dello Russo, N., DiSanti, M. A., Magee-Sauer, K. et al. 2001b, Science, 292, 1334

Mumma, M. J., DiSanti, M. A., Dello Russo, N., Fomenkova, M., Magee-Sauer, K., Kaminski, C. D., & Xie, D. X. 1996, Science, 272, 1310

Mumma, M. J., DiSanti, M. A., Dello Russo, N., Magee-Sauer, K., & Rettig, T. W. 2000, 531, L155

Mumma, M. J., DiSanti, M. A., Dello Russo, N., Magee-Sauer, K., Gibb, E. L., & Novak, R. E. 2003, Adv. Sp. Res., 31, 2563

Mumma, M. J., DiSanti, M. A., Magee-Sauer, K., Bonev, B. P., Villanueva, G. L., Dello Russo, N., Gibb, E. L., Blake, G. A., Lyke, J. E., Campbell, R. D., Aycock, J., Conrad, A., & Hill, G. M. 2005, Science, 310, 270

Mumma, M. J., McLean, I. S., DiSanti, M. A., Larkin, J. E., Dello Russo, N., et al. 2001a, ApJ, 546, 1183.

Paganini, L., Mumma, M. J., Villanueva, G. L., DiSanti, M. A., Bonev, B. P., Lippi, M., & Böhnhardt, H. 2012, ApJ, 748, L13.

Pittichová, J., Woodward, C. E., Kelley, M. S., & Reach, W. T. 2008, ApJ, 136, 1127

Rodgers, S. D., & Charnley, S. B. 1998, ApJ, 501, L227

Rothman, L. S., Gordon, I. E., Barber, R. J., Dothe, H., Gamache, R. R., Goldman, A., Perevalov, V. I., Tashkun, S. A. & Tennyson, J. 2010, JQRST, 111, 2139

Schleicher, D. G. 2009, ApJ, 138, 1062

Schleicher, D. G., Farnham, T. L., & Bair, A. N. 2007, *in* Workshop on Planetary Atmospheres (LPI Contribution No. 1376; Houston, TX: LPI), p. 103

Tielens, A. G. G. M. 1992, *in* Chemistry and Spectroscopy of Interstellar Molecules, University of Tokyo Press, p. 237

Tokunaga, A. T., Toomey, D. W., Carr, J., Hall, D. N., Epps, & H. W. 1990, SPIE, 1235, 131

Villanueva, G. L., Bonev, B. P., Mumma, M. J., Magee-Sauer, K., DiSanti, M. A., Salyk, C., & Blake, G. A. 2006, ApJ, 650, L87

Villanueva, G. L., DiSanti, M. A., & Mumma, M. J. 2012, ApJ, 747, 37

Villanueva, G. L., Mumma, M. J., & Magee-Sauer, K. 2011a, J. Geophys. Res., 116 (E8)

Villanueva, G.L., Mumma, M.J., DiSanti, M.A., Bonev, B.P., Gibb, E.L., Magee-Sauer, K., et al. 2011b, Icarus, 216, 227

Walsh, C., Millar, T. J., & Nomura, H. 2010, ApJ, 722, 1607

Watanabe, N., Nagaoka, A., Shiraki, T., & Kouchi, A. 2004, ApJ, 616, 638

Weaver, H. A., Chin, G., Bockelée-Morvan, D., Crovisier, J., Brooke, T. Y., Cruikshank, D. P., Geballe, T. R., Kim, S. J., & Meier, R. 1999, Icarus, 142, 482

Willacy, K. 2007, ApJ, 660, 441

Willacy, K., & Woods, P. M. 2009, ApJ, 703, 479

Wirström, E. S., Geppert, W. D., Hjalmarson, A., Persson, C. M., Black, J. H., Bergman, P., Millar, T. J., Hamberg, M., & Virgren, E. 2011, A&A, 533, A24

Xu, L.-H., Wang, X., Cronin, T. J., Perry, D. S., Fraser, G. T., & Pine, A. S. 1997, J Mol. Sp. 185, 158

TABLE 1. OBSERVING LOG FOR COMET 21P/GIACOBINI-ZINNER ON UT 2005 JUNE 03 [a]

NIRSPEC Setting	UT Start-End	Molecule (order) [b]	T_{int} [c] [min]
KL1	14:45-15:24	H_2O (26, 27)	24
		C_2H_6 (23)	
		CH_3OH (22, 23)	

[a] R_h = 1.116 AU, Δ = 1.454 AU, $d\Delta/dt$ = -5.4 km s^{-1}, dR_h/dt = -8.8 km s^{-1}. Solar phase angle (β) = 44°.

[b] Quantified primary molecules and NIRSPEC echelle order in which their emissions occur.

[c] Total on-source integration time.

TABLE 2. PRIMARY VOLATILES IN 21P/G-Z ON 2005 JUNE 03.6

Molec.	Order	Band(s)	T_{rot} [a] [K]	Q_{nc} [b] (10^{25} s^{-1})	GF [c]	Q_{tot} [d] (10^{25} s^{-1})
H_2O	26, 27	(e)	$55^{+3}/_{-2}$	2346±33.2(54.5)	1.62±0.059	3800±88
C_2H_6	23	ν_7	[50]	3.25±0.376(0.556)	[1.62]	5.27±0.92
CH_3OH [f]	23	ν_2	[~ 50]	30.1±3.07(4.37)	[1.62]	48.8±7.1
CH_3OH [f]	22	ν_3	$48^{+10}/_{-7}$	28.6±2.82(3.41)		46.3±5.5

[a] Rotational temperatures for H_2O using lines in orders 26 and 27 (Fig. 2), and for CH_3OH from the ν_3 band (Fig. 4). Quantities in square brackets denote adopted values. All uncertainties in the Table are 1σ.

[b] Nucleus-centered production rate based on signal contained in a 9-row extract centered on each emission profile peak, as determined by a best-fit Gauss function. For H_2O (Fig. 1B), the emission is centered on the continuum peak (taken to be centered on the nucleus), while for C_2H_6 and CH_3OH extracts centered -2 rows (~ 400 km) from the nucleus produced the maximum emission intensities (Figs. 1C, 1D). For each tabulated entry, the first uncertainty is the stochastic noise and the second (in parentheses) is the standard error among the lines (i.e., spectral intervals) sampled.

[c] Growth Factor (GF, Eq. 1) used to correct Q_{nc} for slit losses, which are due primarily to atmospheric seeing. For our analysis we assume the value for H_2O applies to the other molecules.

[d] Total or global Q (Eq. 1). For each entry, the uncertainty incorporates the (dominant) standard error in Q_{nc} and the error in GF measured for H_2O (σGF contributes a relatively small amount). Using the GF measured for C_2H_6 (1.90±0.285, based on the profile in Fig. 1C) increases its global Q (and hence the ethane abundance, see Table 3) by ~17 percent, to (6.17±1.40) x 10^{25} s^{-1}; however this is within 1σ of that based on the GF from H_2O and does not change our conclusion of highly depleted C_2H_6 in comet 21P/GZ. Combining CH_3OH from orders 22 and 23 results in $Q_{tot}(CH_3OH)$ = (47.5±4.4) x 10^{25} s^{-1}. For the combined CH_3OH profile (Fig. 1D) we measured GF=1.65±0.241; using this GF increases the combined $Q_{tot}(CH_3OH)$ by only a negligible amount (1.9 percent). For CH_3OH in order 23, σQ_{nc} and σQ_{tot} also include uncertainties in empirical g-factor summed over each interval, based on stochastic noise levels in the 8P/Tuttle residuals (Fig. 3A; see also Table A1).

[e] The 31 H_2O lines included in our analysis arise from eight distinct non-resonant ("hot") bands: 101-110, 111-110, 200-001, 210-110, 200-100, 003-002, 101-001, and 201-200.

[f] For CH_3OH in order 23, Q_{nc} and Q_{tot} correspond to the weighted mean of all intervals in Fig. 3C excluding number 5, due primarily to (unknown) uncertainties in g-factor for the co-measured OH* P12.5 2- line, both for 8P/Tuttle and 21P/GZ as discussed in

§4.2.2. Including interval 5 lowers the global Q for CH_3OH in order 23 by ~18 percent, to (40.1±6.6) x 10^{25} molecules s^{-1}, and lowers the mean Q(CH_3OH) (and hence the abundance of CH_3OH from combining orders 22 and 23) by approximately 10 percent (see Table 3, note f).

TABLE 3. VOLATILE ABUNDANCES IN 21P/G-Z AND OTHER JUPITER FAMILY COMETS

Comet	Year[a]	$\frac{C_2H_6}{H_2O}$[a]	$\frac{CH_3OH}{H_2O}$[a]	Log $\frac{C_2}{OH}$[b]	C_2/OH[q] (%)	$\frac{C_2H_6}{C_2}$[q]
21P/GZ	1998	0.22±0.13[c]				
	1998	< 0.05-0.08[d]	0.9-1.4[d]	-3.41[(1)]	.056	
	1998		1.6±0.4[e]	-3.14[(2)]		
	2005	0.139±0.024[f]	1.25±0.12[f]			2.7
9P/Tempel 1	2005	0.23±0.04[g] 0.55±0.09[h]	1.4±0.2[g] 1.1±0.2[g]	-2.90[(1)] -3.17[(2)]	.097	2.6
73P/SW3-B	2006	<0.3[i]				
73P/SW3-B		0.14±0.01[j]	0.25±0.04[j]	-3.29[(2)]	.051	2.7
73P/SW3-C		0.15±0.04[i]	<0.38[i]			
73P/SW3-C		0.11±0.01[j]	0.21±0.04[j]			
17P/Holmes	2007	1.78±0.26[k]	3.2±0.6[k]	-2.42[(3)]	0.38	5.2
6P/d'Arrest	2008	0.26±0.06[l]	1.99±0.42[l]	-2.37[(1)] -2.90[(2)]	0.28	1.0
103P/Hartley 2	2010	0.75±0.03[m] 0.65±0.09[n]	1.87±0.13[m] 1.72±0.11[n]	-2.36[(1)] -2.59[(2)]	0.35	2.3
10P/Tempel 2	2010	0.39±0.04[p]	1.58±0.23[p]	-2.70[(1)] -2.71[(2)]	0.20	2.1

[a] Year observed (excluding optical observations; see note b) and abundances of ethane and methanol with respect to H_2O = 100 (all uncertainties in the Table represent 1σ, and upper limits are 3σ). Previously published values for $Q(CH_3OH)$ from IR observations using the ν_3 Q-branch intensity are inter-normalized based on g(Q-br) = 1.5 x 10^{-5} ph s^{-1} $molecule^{-1}$ (Villanueva et al. 2012).

[b] Abundances of C_2 are taken from the following papers: (1) A'Hearn et al. 1995, (2) Fink 2009, and (3) Schleicher 2009. With the exception of 17P, the optical observations refer to apparitions different from those listed under "year"; e.g., years of observation for Fink et al.: 21P, 1985; 9P, 1994; 73P, 1990 and 1995; 6P, 1995; 103P, 1997 and 1998; 10P, 1988. A'Hearn et al. 1995 classify comets having -1.22 < $\log(C_2/CN)$ < -0.21, and -4.13 < $\log(C_2/OH)$ < -2.98 as "carbon-chain depleted", and those having -0.09 < $\log(C_2/CN)$ < 0.29 and -2.90 < $\log(C_2/OH)$ < -2.10 as "typical". The values for 17P refer to the mean of 2007 Nov. 01.16, Nov. 20.12, and 2008 Jan. 01.23, during the decline from its spectacular

outburst in late October 2007. Its rapidly evolving coma complicates a comparison of abundances for primary (parent) and product species, and in this sense 17P represents a special case.

[c] Mumma et al. 2000.

[d] Weaver et al. 1999. Their value for $Q(CH_3OH)$ was reported as a 3σ upper limit. It was based on the entire ν_3 band using $g(\nu_3) = 1.5 \times 10^{-4}$ s^{-1}, therefore no re-scaling of production rate from the published value is required.

[e] Biver et al. 2002.

[f] This work. The value listed for C_2H_6 is based on six ν_7 Q-branches (see Figs. 3B and 3D and related discussion in §4.2.3). Including the seventh Q-branch ($^rQ_3$) modifies its abundance to $(0.136 \pm 0.021) \times 10^{-2}$. The value listed for CH_3OH is based on signal in 36 spectral intervals in order 22 (Fig. 4) and 17 spectral intervals (i.e., with number 5 omitted) in order 23 (Figs. 3C and 3E). Including interval 5 in order 23 results in a mean CH_3OH abundance of $(1.12 \pm 0.11) \times 10^{-2}$.

[g] Mumma et al. 2005. The first row corresponds to pre-impact, the second row to the DI ejecta.

[h] DiSanti et al. 2007b.

[i] Villanueva et al. 2006.

[j] Dello Russo et al. 2007 and Kobayashi et al. 2007 reported consistent values for fragment B, from independent measurements.

[k] Dello Russo et al. 2008.

[l] Dello Russo et al. 2009.

[m] Mumma et al. 2011.

[n] Dello Russo et al. 2011.

[p] Paganini et al. 2012.

[q] For comets with multiple entries for $\log(C_2/OH)$, the quantity C_2/OH refers to their mean value. In calculating C_2H_6/C_2, the relation $Q(H_2O) = 1.1 \times Q(OH)$ is assumed. The entry for 21P is based on the value for C_2H_6/H_2O reported here (0.139 percent). The entry for 9P is based on the pre-impact C_2H_6/H_2O (note g). The entry for 73P uses the weighted mean value from the three measurements of C_2H_6/H_2O having 1σ errors ($\sim$ 0.14 percent). The entry for 103P uses the weighted mean value from the two measurements listed for C_2H_6/H_2O.

Figure captions

Fig. 1. A. Schematics showing the observing geometry for 21P/GZ on UT 2005 June 03. Upper: PA of the extended Sun-comet vector (260°) and slit orientation (157°, or 23° W of N) projected onto the sky plane, with the comet located at the origin. Lower: Solar phase angle ($\beta = 44°$) for 21P/G-Z. **B-D.** Comparison of spatial profiles in Comet 21P/G-Z. Projected distance is reckoned with respect to the peak of the observed continuum profile. For comparison, a representative point-spread-function (PSF) is also shown.

Fig. 2. Spectral extracts of H_2O in Comet 21P/G-Z, with best fit fluorescence model, indicating $T_{rot} = 55^{+3}/_{-2}$ K and OPR = 3.00±0.15. The prominent feature near 3485 cm^{-1} (marked with asterisk) corresponds to two blended OH lines (v=1-0: P2.5 1^- and P2.5 1^+, at 3484.59 and 3484.74 cm^{-1}, respectively).

Fig. 3. A. Top traces: Continuum-subtracted residuals from order 23 in 8P/Tuttle, along with our optimized empirical fluorescence model for CH_3OH. Subtracting modeled emissions for C_2H_6, OH, and CH_4 leaves primarily ν_2 emissions (hence labeled "CH_3OH residuals"). Regions marked 'x' contain excess intensity, perhaps due to unaccounted-for CH_3OH ν_9 emissions, and so are omitted from our ν_2 analysis (see Appendix). A stick spectrum for all lines included in the model is also shown, both here and for 21P/GZ, each being multiplied by their appropriate monochromatic transmittances for direct comparison with *observed* emissions. **B.** Top trace: Extracted spectrum in 21P/GZ, with modeled transmittance function convolved to $\lambda/\Delta\lambda = 24{,}000$. Lower traces: Continuum-subtracted spectrum and convolved quantum band model for C_2H_6 ν_7 (with seven Q-branches indicated) and empirical model for OH prompt emission. **C.** Residual emission spectrum after subtraction of modeled C_2H_6 and OH, with our new empirical model super-imposed. **D.** Production rates derived from individual C_2H_6 Q-branches at (adopted) T_{rot} of 50 K, and the mean Q_{tot} based on points 2 through 6 (dashed line). **E.** Similar graphic for the 18 spectral intervals used in our analysis of CH_3OH in order 23 from panel C. The mean Q_{tot} excludes point number 5, as discussed in the text.

Fig. 4. A. Spectral extracts of order 22, showing emissions from the ν_3 band of CH_3OH in Comet 21P/G-Z, with the Q-branch indicated. **B.** Measured (total) production rates

derived from each of the 36 spectral intervals delineated in panel A, with that from the Q-branch indicated (Q_{br}). **C**. Best-fit slope over a range of rotational temperatures, indicating optimal T_{rot} (slope = 0) and $\pm 1\sigma$ uncertainties (these are based on corresponding uncertainties in slope; cf. DiSanti et al. 2006 for detailed formalism).

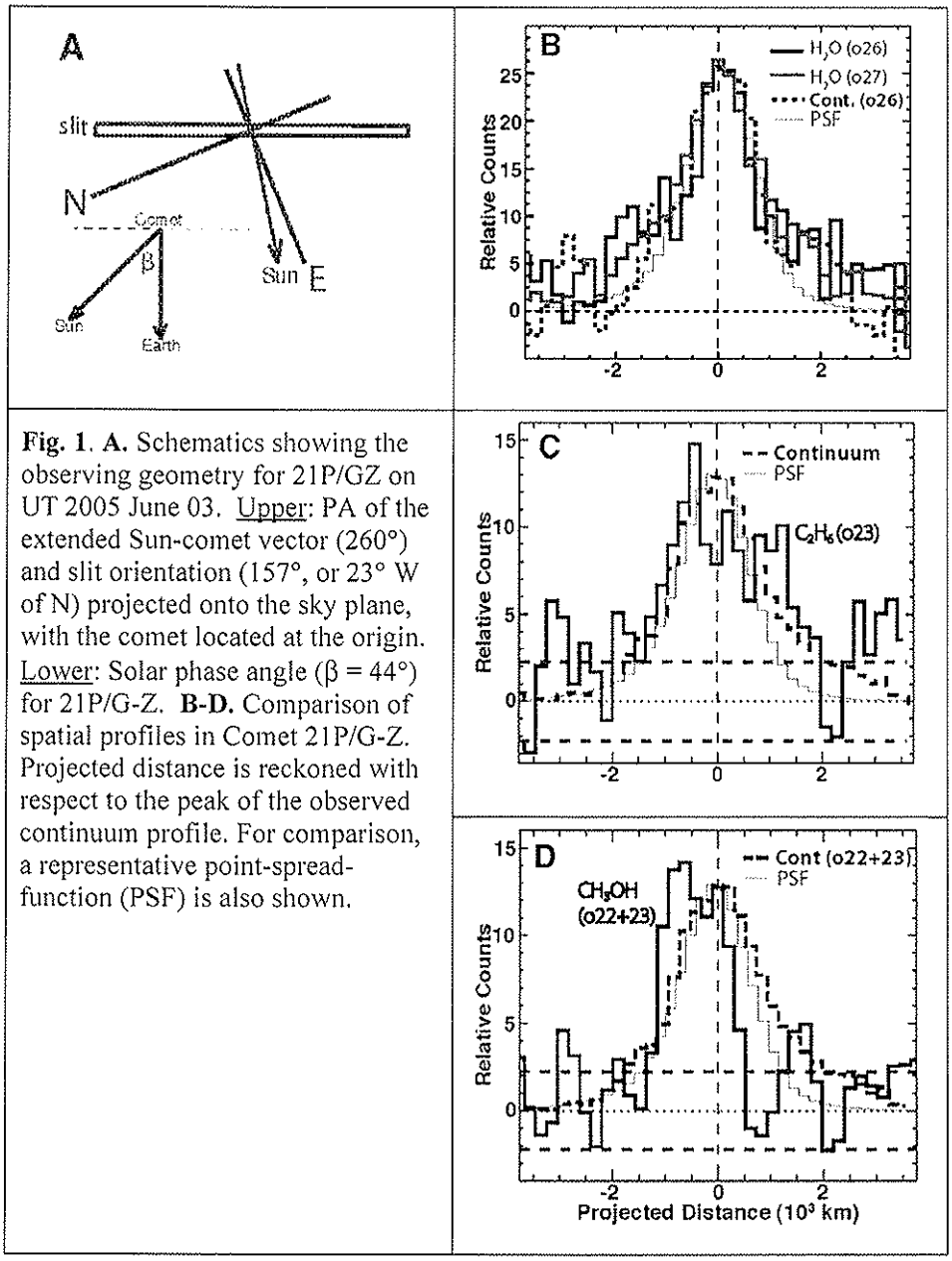

Fig. 1. A. Schematics showing the observing geometry for 21P/GZ on UT 2005 June 03. Upper: PA of the extended Sun-comet vector (260°) and slit orientation (157°, or 23° W of N) projected onto the sky plane, with the comet located at the origin. Lower: Solar phase angle (β = 44°) for 21P/G-Z. **B-D.** Comparison of spatial profiles in Comet 21P/G-Z. Projected distance is reckoned with respect to the peak of the observed continuum profile. For comparison, a representative point-spread-function (PSF) is also shown.

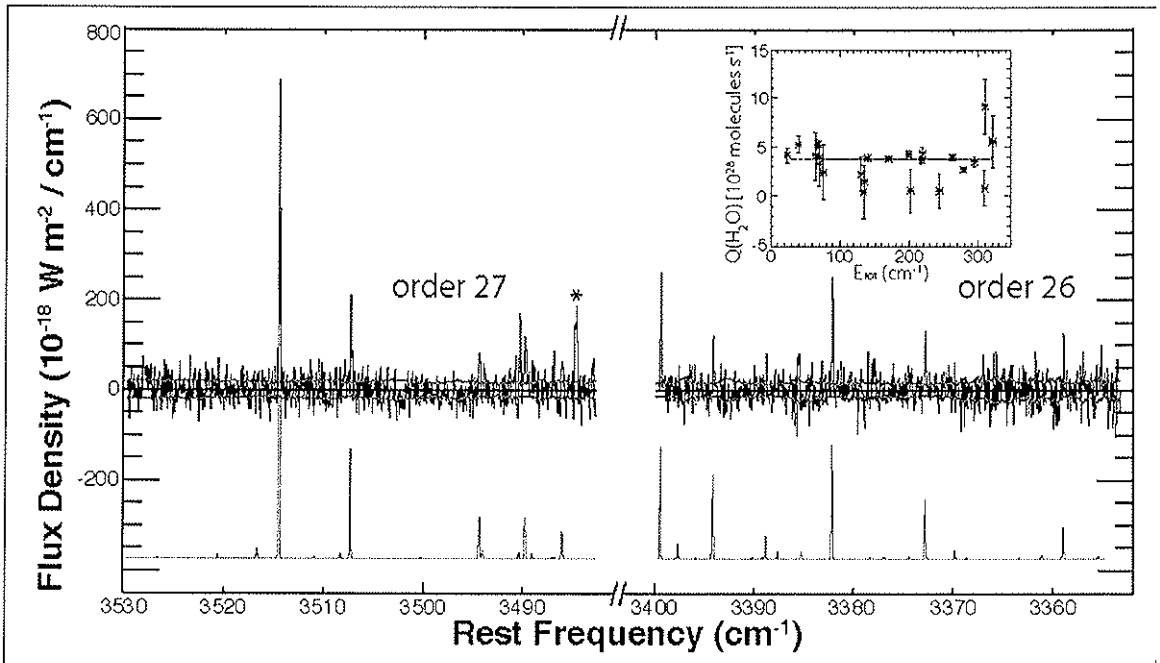

Fig. 2. Spectral extracts of H_2O in Comet 21P/G-Z, with best fit fluorescence model, indicating T_{rot} = $55^{+3}/_{-2}$ K and OPR = 3.00±0.15. The prominent feature near 3485 cm^{-1} (marked with asterisk) corresponds to two blended OH lines (v=1-0: P2.5 1$^-$ and P2.5 1$^+$, at 3484.59 and 3484.74 cm^{-1}, respectively).

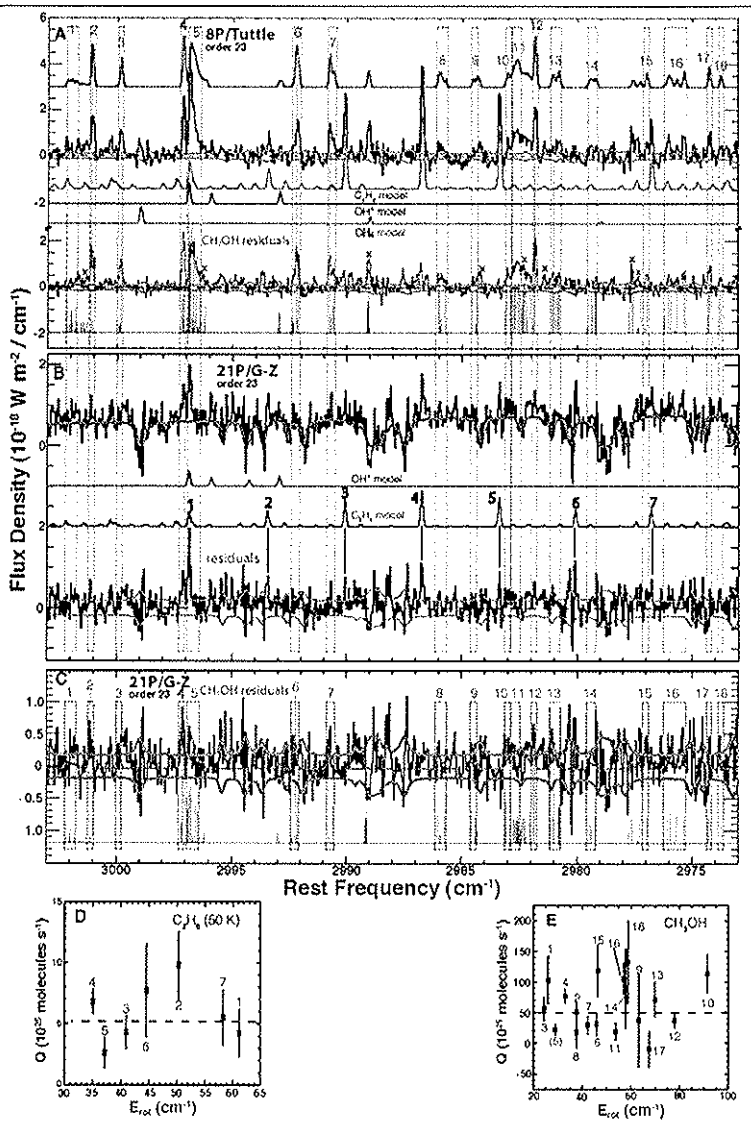

Fig. 3. A. Top traces: Continuum-subtracted residuals from order 23 in 8P/Tuttle, along with our optimized empirical fluorescence model for CH_3OH. Subtracting modeled emissions for C_2H_6, OH, and CH_4 leaves primarily ν_2 emissions (hence labeled "CH_3OH residuals"). Regions marked 'x' contain excess intensity, perhaps due to unaccounted-for CH_3OH ν_9 emissions, and so are omitted from our ν_2 analysis (see Appendix). A stick spectrum for all lines included in the model is also shown, both here and for 21P/GZ, each being multiplied by their appropriate monochromatic transmittances for direct comparison with *observed* emissions. **B**. Top trace: Extracted spectrum in 21P/GZ, with modeled transmittance function convolved to $\lambda/\Delta\lambda$ = 24,000. Lower traces: Continuum-subtracted spectrum and convolved quantum band model for C_2H_6 ν_7 (with seven Q-branches indicated) and empirical model for OH prompt emission. **C**. Residual emission spectrum after subtraction of modeled C_2H_6 and OH, with our new empirical model super-imposed. **D**. Production rates derived from individual C_2H_6 Q-branches at (adopted) T_{rot} of 50 K, and the mean Q_{tot} based on points 2 through 6 (dashed line). **E**. Similar graphic for the 18 spectral intervals used in our analysis of CH_3OH in order 23 from panel C. The mean Q_{tot} excludes point number 5, as discussed in the text.

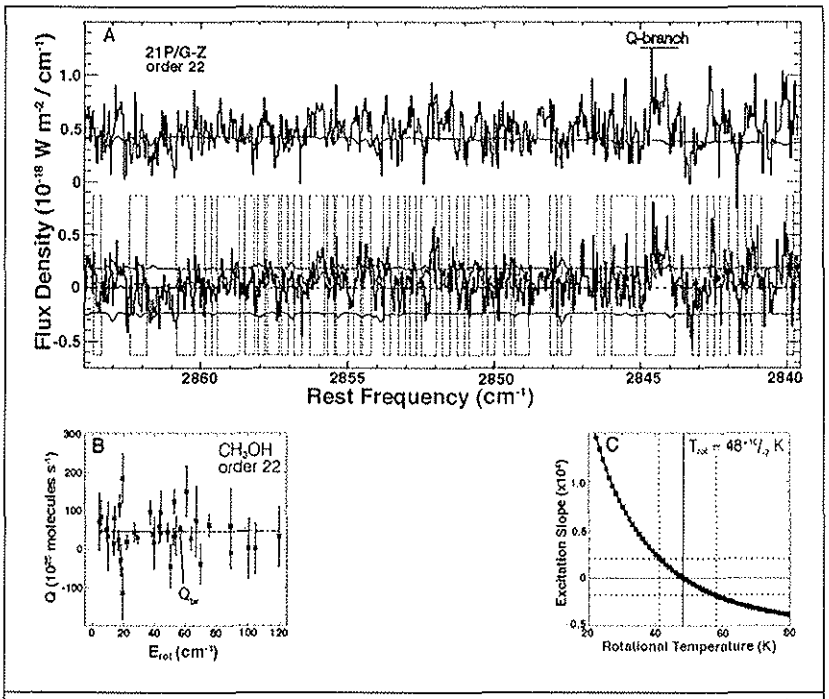

Fig. 4. **A**. Spectral extracts of order 22, showing emissions from the ν_3 band of CH_3OH in Comet 21P/G-Z, with the Q-branch indicated. **B**. Measured (total) production rates derived from each of the 36 spectral intervals delineated in panel A, with that from the Q-branch indicated (Q_{br}). **C**. Best-fit slope over a range of rotational temperatures, indicating optimal T_{rot} (slope = 0) and $\pm 1\sigma$ uncertainties (these are based on corresponding uncertainties in slope; cf. DiSanti et al. 2006 for detailed formalism).

Appendix. Application of the CH_3OH Empirical ν_2 Band Model to Comet GZ

For our empirical model of the CH_3OH ν_2 band, we adopt notation according to the G_6 molecular symmetry group, as this takes into account the large amplitude torsional tunneling between the three equivalent CH_3 orientations relative to OH (Xu et al. 1997; Xu et al. 2008). Under the G_6 group representation, the rotational structure is described using three quantum numbers (J, K, *l*), where J (≥ 0) is the usual total angular momentum, K is its projection along the symmetry a-axis of the molecule (such that $0 \leq K \leq J$), and *l* is related to the parity of the states involved in the transition. The G_6 symmetry group uses the representations A_1, A_2, E_1 and E_2, where subscript "1" is associated with positive parity of a ro-vibrational state and "2" with negative parity, thereby leading to the representations A^+, A^-, E^+, and E^-. Following Mekhtiev et al. (1999), we differentiate between E^+ to E^- states by denoting the latter using negative K values. Using the standard convention, a single-prime denotes the upper vibrational state ($v = \nu_2$) and a double-prime denotes the lower (ground) vibrational state ($v = 0$). Then, for example (see Table A.1), the designation A^+ (1->0)P4 corresponds to J' = 3, K' = 1, *l*' = 1, and J" = 4, K" = 0, *l*" = 1, while E (-1->-2)R5 corresponds to J' = 6, K' = -1, *l*' = 2, and J" = 5, K" = -2, *l*" = 2.

To establish spectral intervals for determining the CH_3OH production rate using our empirical model, we first identified regions in the order 23 spectrum of Comet 8P/Tuttle having residual intensity after accounting for emissions due to C_2H_6, OH, and CH_4 (see Fig. 3A, in particular the bottom trace labeled "CH_3OH residuals"). We next incorporated line assignments and frequencies from the compilation in Xu et al. (1997) based on supersonic (jet) spectra of CH_3OH measured at low temperature (~ 17 K). We assigned fluorescence g-factors for lines contained in each spectral interval such that their sum reproduced the nucleus-centered production rate ($Q_{nc,int}$ in Eq. 2) retrieved for 8P/Tuttle ($=2.90 \times 10^{26}$ molecules s^{-1}) based on application of our recently published ν_3 quantum band model to the residuals shown in Fig. 4A for order 22 (this "revised" Q_{tot}, which includes GF = 1.5 as discussed in Bonev et al. 2008, is presented in Table 4 of Villanueva et al. 2012; also see §3.2 in the present paper).

Rigorous calculation of line g-factors requires a full quantum mechanical fluorescence model for the ν_2 band, in which solar pumps from all (dipole-allowed) contributing levels in the ground vibrational state ($v = 0$) into each upper level (in $v = \nu_2$) are summed (with potential cascades from higher ro-vibrational levels included). Each particular line g-factor is then given by this summed pump rate multiplied by the rotational branching ratio for the line in question. However, such a treatment is beyond the scope of the present paper.

Instead, in our empirical treatment, we preformed checks on lines having similar rotational designation (J, K) and symmetry (A, E). This approach provided more consistent g-factors, and also provided insights as to which spectral regions *not* to include in our treatment. To accomplish this, we examined the intensities of spectral lines, which for a given transition can be expressed as a proportionality with respect to line parameters and rotational temperature:

$$S_{line} \propto \frac{\nu}{\nu_0} L_{HL}[1 - \exp(-hc\nu/kT)][(2J+1)\exp(-hcE/kT)] \qquad \text{(A1)}$$

Here, and in the formulae below, ν is the line frequency (cm^{-1}), ν_0 is the band frequency (2999 cm^{-1}), J, K and E (cm^{-1}) are respectively lower state rotational quantum numbers and energy (denoted "E_{low}" in the table below, and taken from Mekhtiev et al. 1999), T is rotational temperature, and L_{HL} is the Hönl-London factor. For a perpendicular band such as ν_2, the intensity of which is dominated by lines having 'A' symmetry in b-type sub-bands (for which $\Delta K = \pm 1$; e.g., see Xu et al. 1997), L_{HL} is given by:

$$L_{HL} = \frac{(J-1 \mp K)(J \mp K)}{J(2J+1)} \text{ for } \Delta J = -1 \text{ (P-branch lines)},$$

$$L_{HL} = \frac{(J+1 \pm K)(J \mp K)}{J(J+1)} \text{ for } \Delta J = 0 \text{ (Q-branch lines)}, \qquad \text{(A2)}$$

$$L_{HL} = \frac{(J+2 \pm K)(J+1 \pm K)}{(J+1)(2J+1)} \text{ for } \Delta J = +1 \text{ (R-branch lines)},$$

where the upper sign in each equation refers to ΔK (= K_{upper} –> K_{lower}) = +1, and the lower sign refers to $\Delta K = -1$ (Herzberg 1945, p. 426).

An example is provided by P-branch lines in the A($\Delta K = 1 \rightarrow 2$) sub-band. In the Comet 8P/Tuttle "CH_3OH residual" spectrum (Fig. 3A), the intensity contained in the left-most (highest frequency) peak in interval 16 (near 2976.0 cm^{-1}) is dominated by $A^{-/+ \rightarrow -/+}$ P4 components. The corresponding P3 components at ~ 2977.6 cm^{-1} coincide approximately with a feature having strong residual intensity (additionally, a second feature near 2977.4 cm^{-1} has lower intensity but no viable corresponding ν_2 line). Using the above equations (and assuming T = 50 K) suggests an intensity ratio P3/P4 = 1.07, and this is reflected in the model shown in Fig. 3. [We note that the modeled "P3" feature appears weaker than the feature in interval 16, however this results from its relatively poorer transmittance (~ 50 %) compared with that of the "P4" feature (~ 95 %).] However, to account for the intensity in the CH_3OH residuals near 2977.6 cm^{-1} requires an unrealistically large ratio of ~ 1.8, and we therefore exclude this region from our analysis. Similar reasoning pertains to other excluded spectral regions (marked 'x' in Fig. 3A), and this approach will be used as our empirical model is improved through extension to other comets in our database encompassing a range of rotational temperatures. Table A1 provides a summary of our empirical model as applied to Comet 21P/Giacobini-Zinner.

Table A1. CH_3OH ν_2 empirical model results for 21P/Giacobini-Zinner on UT 2005 June 03

or	ν_{max} - ν_{min} [a]	Rot ID [b]	Rest ν [b]		E_{low} [b]	F_{line} [c]	g-fac [d]	Q [e]
	(cm^{-1})		tabulated	wtd mean	(cm^{-1})	(10^{-19} W m^{-2})	(10^{-7} s^{-1})	(10^{25} s^{-1})
1	3002.18 - 3001.70	A^+ (0->0) P3	3002.154		9.68			
		A^+ (1->0) P4	3002.121		16.13			
		E(1->2) R6	3002.054		49.35			
		E(1->0) R2	3001.975		13.96			
		A^+/-(3->3) Q	3001.940		~50.00			
		E(-1-> -2) R5	3001.905		42.21			
		E[-3] R6	3001.799		11.73			
		A^- (1->1) R1	3001.775		14.90			
		A^+ (0->1) R2	3001.777		77.47			
		A^+ (1->1) R1	3001.735		11.70			
				3001.954	**25.65**	**0.831±0.284**	**15.72±1.91**	**11.10±3.79(4.04)**
2	3001.21 - 3000.97	E(-1->0)Q	3001.080		38.50			
		E(0-0)R3	3001.042		18.80			
				3001.079	**37.65**	**0.790±0.210**	**32.69±1.51**	**50.73±13.49(13.82)**
3	3000.01 - 2999.77	A^+ [2->1]P4	3000.002		26.10			
		A^+/-(2->2)R5	2999.912		50.41			
		E(-1-> -1)P4'	2999.894		50.41			
		E(-1-> -1)P4"	2999.836		78.34			
		E(0-> -1)Q	2999.83		20.32			
				2999.854	**24.31**	**0.625±0.202**	**23.36±1.36**	**56.19±18.21(18.61)**
4	2997.31 - 2997.07	E(1->2)R3	2997.250		25.14			
		A^+ (0-1)P7	2997.161		45.16			
		E(1->0)Q	2997.14		32.51			
		E(0->1)R4	2997.130		30.76			
		E(-2->-2)P3	2997.116		27.68			
				2997.139	**33.02**	**1.355±0.191**	**37.21±1.30**	**76.59±10.82(11.49)**

5	2996.95 - 2996.42		A+·>·(1->0)Q2	2996.870		43.69			
			A+·>·(1->0)Q1	2996.847		11.73			
			A+·>·(1->0)Q3	2996.811		14.99			
			A+·>·(1->0)Q4	2996.763		19.87			
			E(-1-> -1)P6''	2996.715		26.38			
			A+·>·(1->0)Q5	2996.702		37.75			
			A+/·>+/·(2->2)R3	2996.674		34.52			
			E(0--> -1)P2'	2996.639		35.89			
			A+·>·(1->0)Q6	2996.626		35.89			
			E(-1-> -1)P6'	2996.626		44.28			
			E(0--> -1)P2''	2996.611		8.72			
			E(2->2)P5	2996.542		8.72			
			A+·>·(1->0)Q7	2996.537		37.75			
			E(1->1)R2	2996.470		55.67			
			A+·>·(0->1)Q8	2996.431		39.67			
					2996.675	**32.01**	**0.809±0.289**	**85.88±1.98**	**19.82±7.08(7.13)**
6	2992.44 - 2992.08		A·(1-->2}R5	2992.389		50.41			
			E(0-1)R1	2992.324		16.24			
			E(1-0)P3	2992.294		18.80			
			E(-1-> -2)Q	2992.23		55.46			
			A+(1->1)P4	2992.153		26.10			
			A+(0->1)P3	2992.131		19.70			
					2992.224	**45.85**	**0.689±0.409**	**45.83±2.67**	**31.68±18.81(18.94)**
7	2990.89 - 2990.53		E(1->2)Q	2990.76		48.69			
			A·(1->2)R4	2990.693		42.34			
			E(1->0)P4	2990.684		25.25			
			A+(1->1)P5	2990.580		26.10			
			A+(0->1)P4	2990.575		34.10			
					2990.715	**42.30**	**0.511±0.246**	**36.60±1.67**	**29.43±14.19(14.29)**
8	2986.14 - 2985.65		A+(0->1)P7	2986.017		54.89			
			E(-2-> -3)R5	2985.956		25.14			
			E(1->2)P3	2985.956		67.79			
			E(0->1)P2'	2985.887		19.47			

			E(1->0)P7	2985.859		19.47			
			E(0->1)P2"	2985.859		54.27			
			E(-1-> -2)P4	2985.708		34.14			
					2985.907	**37.69**	**0.200±0.279**	**23.36±1.90**	**18.10±25.19(25.24)**
9	2984.62 - 2984.33		A+(0->1)P8	2984.524		67.68			
			E(-2-> -3)R4	2984.382		42.35			
			E(1->2)P4	2984.342		31.60			
					2984.403	**50.99**	**0.157±0.317**	**13.61±1.76**	**24.32±49.23(49.33)**
10	2983.14 - 2982.90		A···+(1->2)Q10	2983.131		96.13			
			A···+(1->2)Q9	2983.010		98.82			
			A+(0-->1)P9	2983.044		82.07			
			A···+(1->2)Q8	2982.898		84.30			
					2983.019	**92.44**	**0.755±0.206**	**17.91±1.43**	**89.14±24.31(25.54)**
11	2982.86 - 2982.48		A+···(1->2)Q7	2982.797		53.27			
			E(-2-> -3)R3	2982.797		71.39			
			E(1->2)P5	2982.726		39.67			
			A+···(1->2)Q6	2982.705		60.10			
			E(0->1)P4	2982.635		81.64			
			E(1->0)P9	2982.635		30.76			
			A+···(1->2)Q5	2982.624		50.41			
			A+···(1->2)Q4	2982.555		51.89			
			E(-1-> -2)P6'	2982.573		42.35			
			E(-1-> -2)P6"	2982.487		35.89			
			A+···(1->2)Q3	2982.501		51.89			
					2982.647	**49.90**	**0.444±0.320**	**50.57±1.89**	**18.55±13.39(13.43)**
12	2981.99 - 2981.74		E(1-1)P6	2981.941		48.51			
			A+···(3->2)Q	2981.86		81.24			
			A···+(3->2)Q	2981.83		76.24			
					2981.848	**78.03**	**0.683±0.206**	**39.17±1.40**	**36.89±11.14(11.30)**
13	2981.21 - 2980.76		E(1->2)P6	2981.106		49.35			
			E(0->1)P5	2981.012		38.83			
			E(-1-> -2)Q*	2981.04		30.00			

			E(-1-> -2)P7	2980.924		63.19			
			A^{-}->$^{+}$(3->4)Q	2980.825		115.1			
			A^{+}->$^{-}$(3->4)Q	2980.793		103.8			
					2980.918	**60.21**	**1.512±0.666**	**44.96±4.91**	**71.10±31.33(32.38)**
14	2979.56 - 2979.15		E(0-> -1)P12	2979.549		129.6			
			E(1->2)P7	2979.479		60.65			
			E(0->1)P6	2979.380		48.51			
			E(-1-> -2)P8	2979.332		76.10			
			A^{+}(1->2)P2	2979.181		31.05			
			A^{-}(1->2)P2	2979.204		31.05			
					2979.352	**54.16**	**1.638±0.641**	**24.33±3.06**	**142.40±58.34(61.25)**
15	2977.16 - 2976.92		E(1->1)P9	2977.044		87.24			
			A^{-}(2->3)P3	2976.965		44.29			
			A^{+}(2->3)P3	2976.966		44.29			
					2976.973	**46.42**	**0.637±0.224**	**11.36±1.58**	**118.70±41.78(45.13)**
16	2976.25 - 2975.30		E(-1-> -2)P10	2976.192		88.09			
			E(0->1)P8	2976.043		72.72			
			A^{-}(1->2)P4	2976.047		42.34			
			A^{+}(1->2)P4	2975.909		42.35			
			A^{+}(2->2)P9	2975.750		98.82			
			A^{-}(2->2)P9	2975.735		98.80			
			E(2->3)P7	2975.656		78.34			
			A^{-}(2->3)P4	2975.356		50.75			
			A^{+}(2->3)P4	2975.357		50.75			
					2975.732	**57.00**	**1.800±0.422**	**36.29±2.81**	**104.98±24.61(26.20)**
17	2974.35 - 2974.14		E (0-->1)P9	2974.282		87.24			
			A^{+}(1->2)P4	2974.260		50.41			
			A^{+}(3->4)P4	2974.240		71.98			
			A^{-}(3->4)P4	2974.239		71.98			
					2974.251	**67.48**	**-0.079±0.222**	**16.63±1.95**	**-10.01±28.30(28.33)**
18	2973.89 - 2973.64		A^{-}(2->3)P5	2973.748		58.81			
			A^{+}(2->3)P5	2973.751		58.81			

					2973.750	**58.81**	**0.544±0.275**	**8.70±1.70**	**132.58±67.07(72.06)**

[a] Range of rest frequencies (cm^{-1}) encompassed by each spectral interval in Fig. 3.

[b] Rotational designation and tabulated rest frequencies are taken from Xu et al. 1997. The asterisk in interval 13 denotes an E-type Q-branch of the ν_9 band; its frequency and energy are only approximate. The heading "wtd mean" for each spectral interval denotes the mean rest frequency weighted by contributing line-by-line empirical g-factors (including atmospheric transmittance at the Doppler shifted line center, using Δ-dot = -5.42 km s^{-1}), based on the "CH_3OH residuals" in 8P/Tuttle (bottom trace in Fig. 3A). Equations SOM 1 and 2 were used as a guide for modeling line intensities for lines having similar rotational designation and symmetry, as discussed above. Lower state energies (E_{low}) were taken from Mekhtiev et al. (1999).

[c] Nucleus-centered line flux and 1σ stochastic error for each interval, corrected for weighted mean atmospheric transmittance.

[d] Summed fluorescence-efficiency g-factor (at R_h = 1 AU) for each interval. Uncertainties in g represent 1σ and are based on the stochastic noise summed over for each spectral interval in the 8P/Tuttle order 23 spectrum.

[e] Global (total) production rate based on the signal contained in each interval. The first uncertainty incorporates the 1σ error in line flux (plus σGF, which adds only a minor contribution). The second uncertainty (in parentheses) includes these errors plus the 1σ uncertainty in empirical g-factor for each interval.

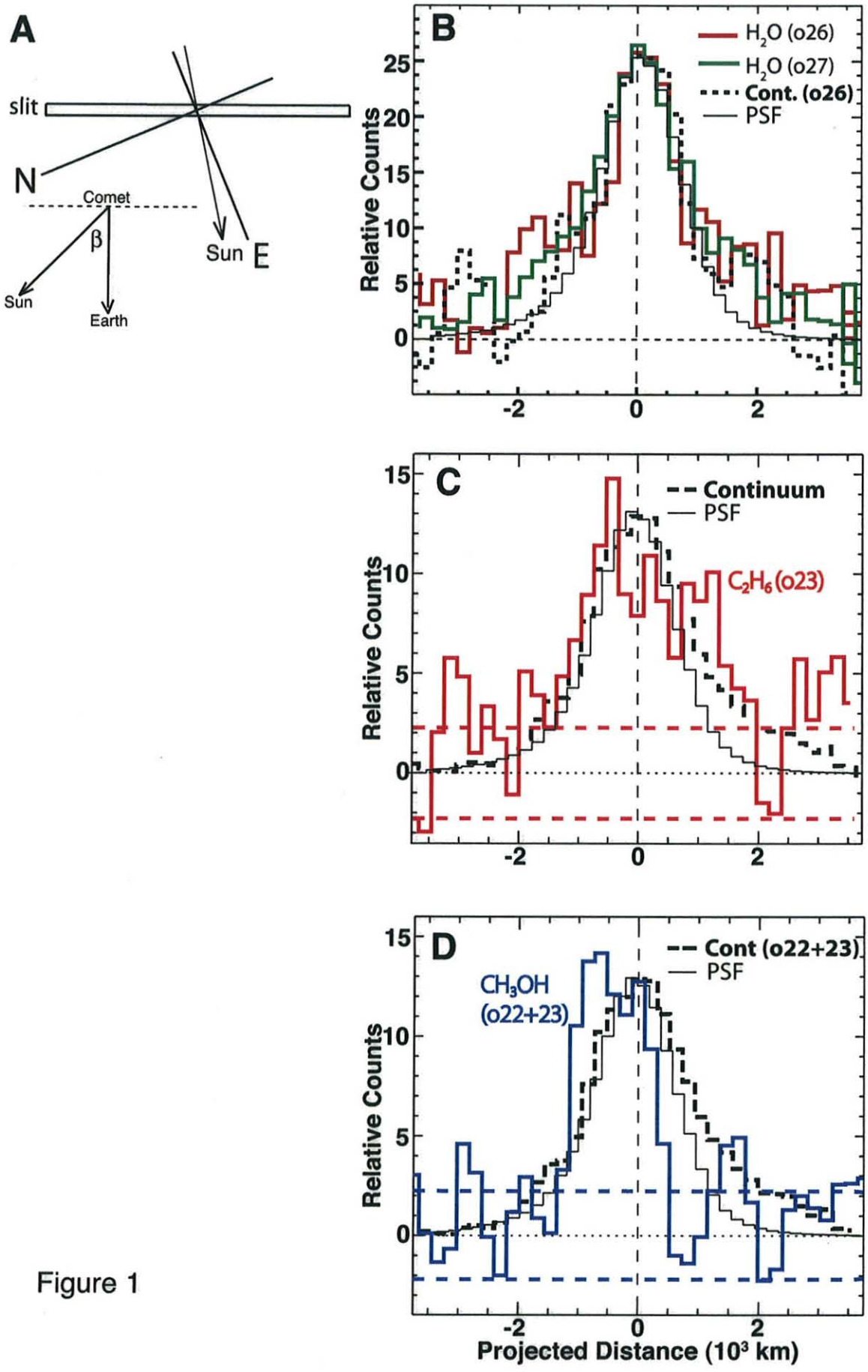
A
slit
N
Comet
β
Sun
E
Sun
Earth
B
H2O (o26)
H2O (o27)
Cont. (o26)
PSF
Relative Counts
C
Continuum
PSF
C2H6 (o23)
Relative Counts
D
Cont (o22+23)
PSF
CH3OH
(o22+23)
Relative Counts
Projected Distance (10³ km)

Figure 1

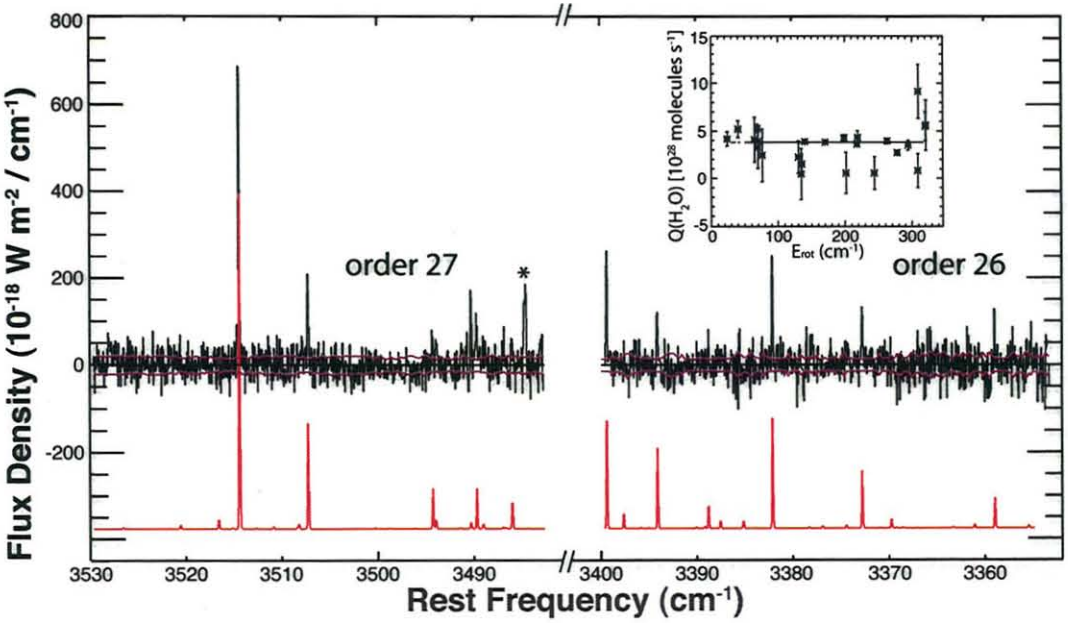
Flux Density (10^{-18} W m^{-2} / cm^{-1})
Rest Frequency (cm^{-1})
order 27
order 26
*
Q(H$_2$O) [10^{28} molecules s^{-1}]
E_{rot} (cm^{-1})

Figure 2

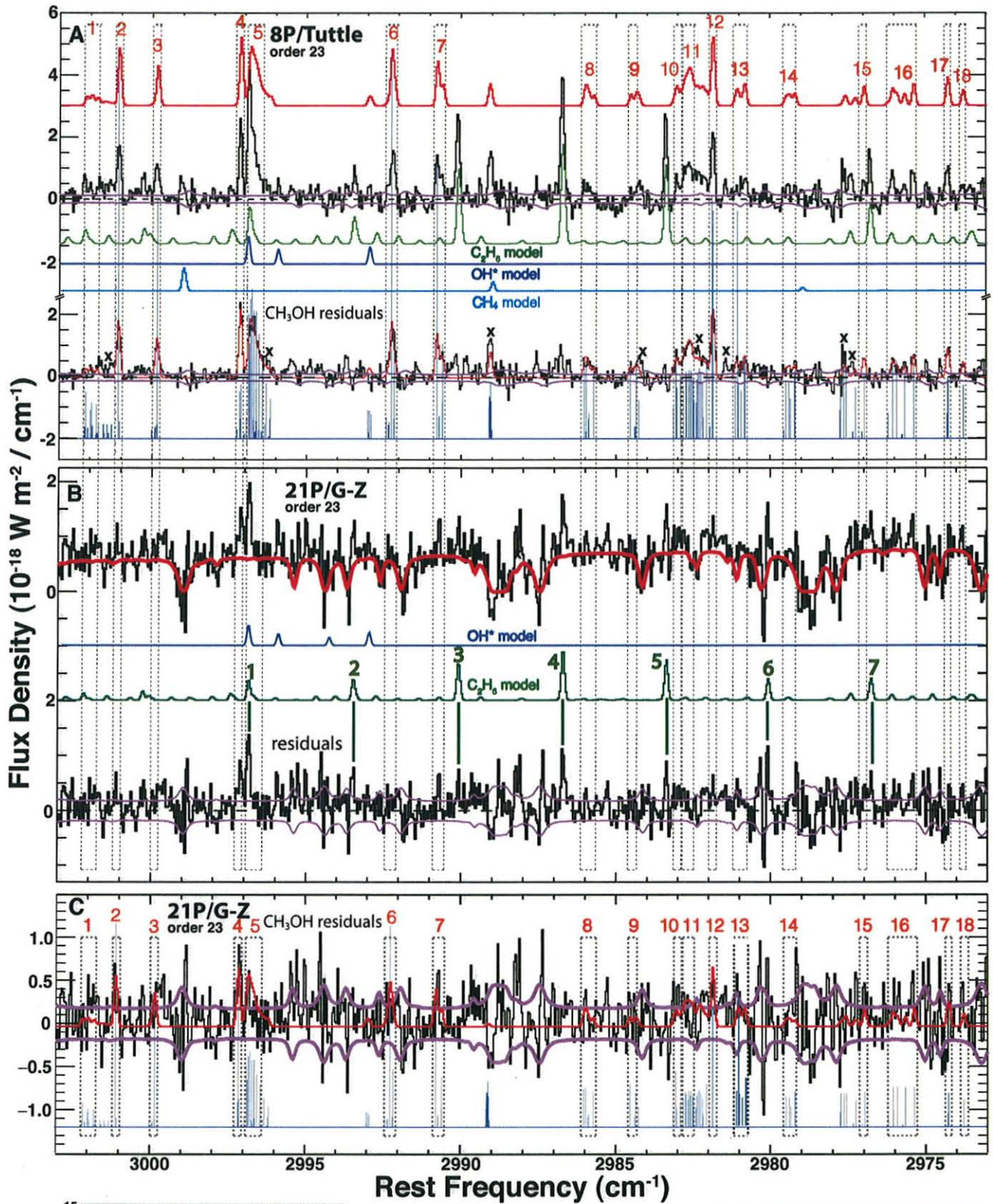
A
8P/Tuttle
order 23
C2H6 model
OH* model
CH4 model
CH3OH residuals
B
21P/G-Z
order 23
OH* model
C2H6 model
residuals
C
21P/G-Z
order 23
CH3OH residuals
Flux Density (10-18 W m-2 / cm-1)
Rest Frequency (cm-1)

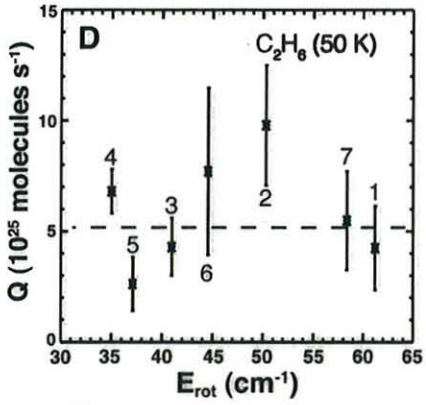
D
C2H6 (50 K)
Q (10^25 molecules s-1)
Erot (cm-1)

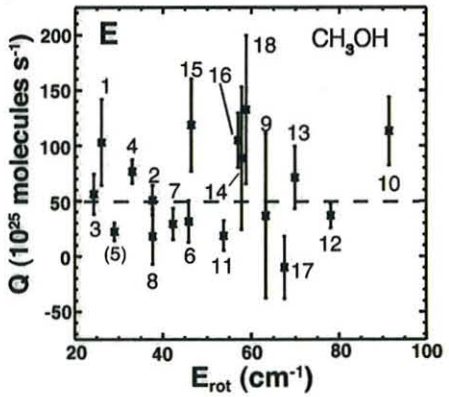
E
CH3OH
Q (10^25 molecules s-1)
Erot (cm-1)

Figure 3

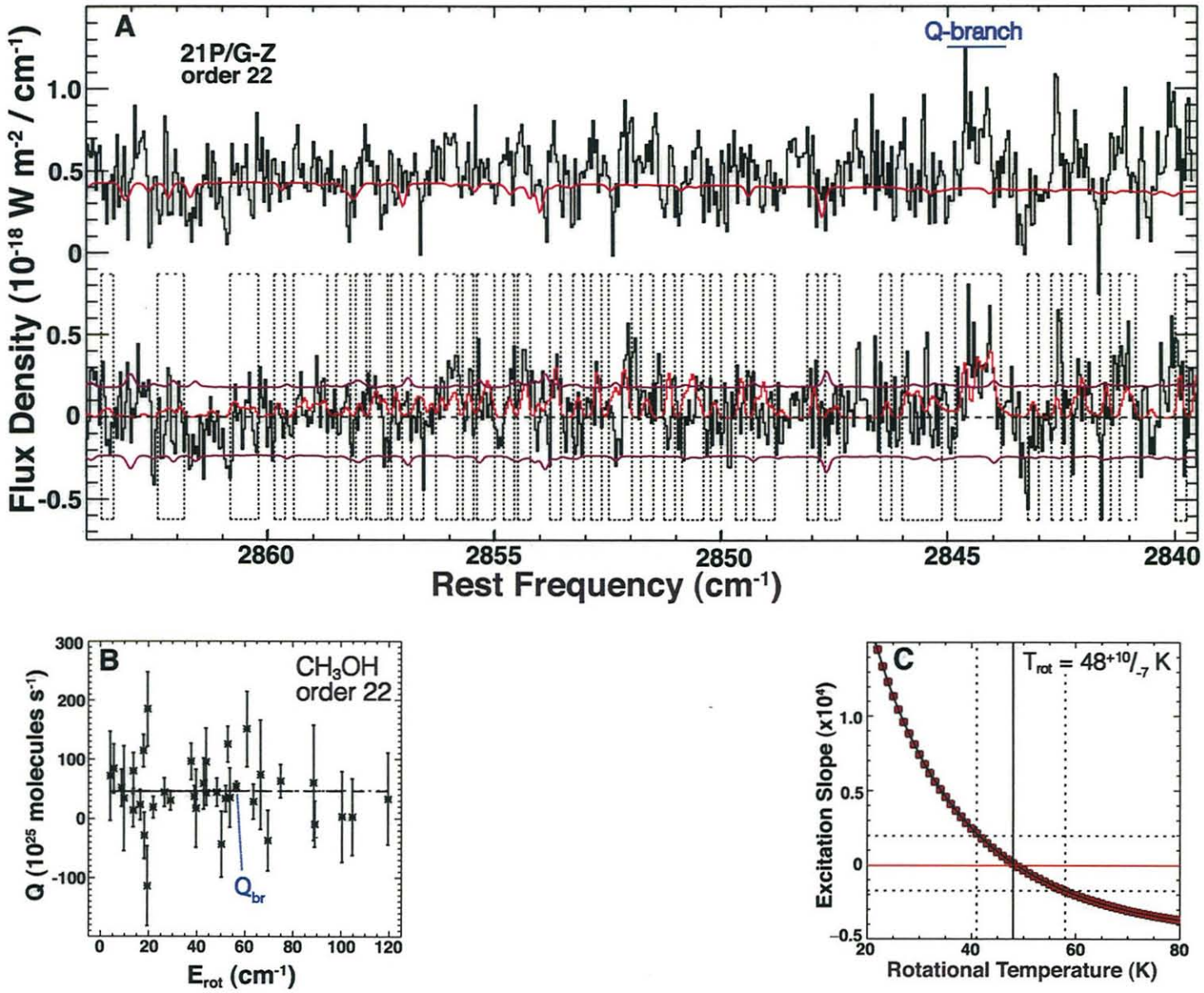
A
21P/G-Z
order 22
Q-branch
Flux Density (10^{-18} W m^{-2} / cm^{-1})
1.0
0.5
0
0.5
0
-0.5
2860
2855
2850
2845
2840
Rest Frequency (cm^{-1})

B
CH_3OH
order 22
Q (10^{25} molecules s^{-1})
300
200
100
0
-100
Q_{br}
0
20
40
60
80
100
120
E_{rot} (cm^{-1})

C
$T_{rot} = 48^{+10}/_{-7}$ K
Excitation Slope (x10^4)
1.0
0.5
0
-0.5
20
40
60
80
Rotational Temperature (K)

Figure 4